3D TOPOLOGY OPTIMIZATION WITH FATIGUE CONSTRAINTS

- JOACHIM E. K. HERSBØLL

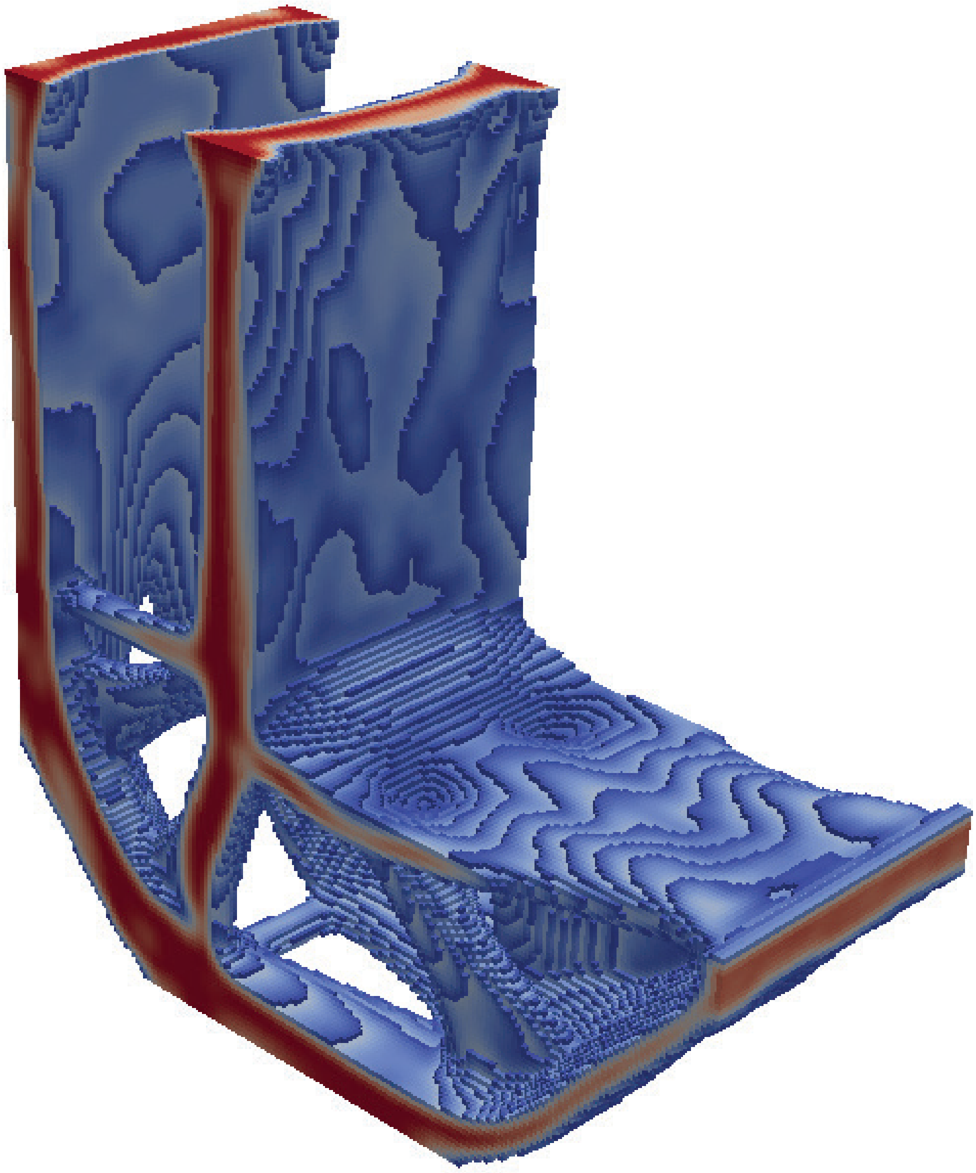

AALBORG UNIVERSITY
DENMARK

Department of Mechanical and Manufacturing Engineering
Fibigerstraede 16
9220 Aalborg Øst

Title:

3D Topology Optimization with Fatigue Constraints

Project:

DMS4

Period:

02/02/18 - 01/06/18

Group:

Fib14/23f

Member:

Joachim E. K Hersbøll

Supervisor:

Erik Lund

Submission: 01/06/2018

Synopsis:

This project concern the formulation and execution of large-scale 3D topology optimization considering a minimum mass objective, while being subjected to yield and or fatigue constraints. The fatigue constraint is formulated considering proportional loading with a variable amplitude. An equivalent uniaxial amplitude stress and S-N curves are used to estimate the number of cycles until failure, which then by employing Palmgren-Miners linear damage hypothesis establishes the fatigue constraint. The established formulation is then illustrated on a number of benchmark examples, highlighting the characteristics of considering fatigue constraints.

Preface

This is the master thesis written by Joachim Hersbøll at the 4^{th} semester of the master's program Design of Mechanical Systems at Aalborg University. It covers 3D topology optimization considering a minimum mass objective while being subjected to yield and fatigue constraints. I would like to express my gratitude and appreciation for my classmates who have greatly increased the enjoyment of studying at AAU, as well as my family and girlfriend who has always supported and encouraged me. Lastly, I would like thank my supervisor Erik Lund and Jacob Oest for the inspiration, discussions and guidance during this master's thesis.

Reading and Formalities

References are notated based on the Harvard method and a detailed bibliography list is present after the last chapter. By use of the Harvard method, a reference is displayed as: (Surname of author(s), year of publication).

Equations, figures, sections are numerated according to chapters, i.e. a reference to the first figure in chapter one is displayed as 1.1, the second 1.2 etc. For numbered equations, the number is displayed in the right margin of the page, next to the respective equations. Figure numbers are displayed underneath the corresponding figure, along with a brief description of what is illustrated.

The following software have been used:

- Matlab Release 2017a
- Eclipse Oxygen.2 Release (4.7.2)
- Texmaker 5.0.2

Aalborg Universitet, June 1st, 2018

Joachim E. K. Hersbøll

Abstract

This thesis concern the formulation and execution of structural optimization by the use of topology optimization in both 2D and 3D, for large-scale optimization problems dependent on many variables. Topology optimization strives to find the optimal distribution of material for a specific domain, given an objective and subjected to a set of constraints. Here, the objective is to minimize the mass, while being subjected yield and/or fatigue constraints.

First chapter of this thesis deals with the general issues of topology optimization. These issues that contain checkerboarding, mesh dependent solutions, minimum length scale and solid/void structures, are illustrated for the classic topology optimization formulation which seeks to minimize the compliance while being subjected to a volume constraint.

Both the yield and fatigue constraints are dependent upon the stresses which occur in a structure subjected to loading. Thus, the second chapter considers the specific challenges associated with stress based constraints in topology optimization. Initially, the formulation of stress constraint within the context of density based topology optimization is examined, followed by well known issue of singular optima. The problem of singular optima is here solved using the qp approach. Due to the local nature of stress based constraints, and since this thesis is concerning large-scale optimization problems, will the associated computational consequences be addressed by employing an aggregate function. Based on the aforementioned is it possible to formulate a yield constraint, using the von Mises yield criterion.

Besides the yield constraint, is a constraint based on the fatigue of the structure is also formulated. Like yielding, fatigue does depend on the stresses in the structure, thus the previous mentioned challenges are likewise relevant and solved with the same techniques.

The fatigue constraint is formulated based on assumptions of proportional loading with a variable amplitude, as well as linear elastic deformation in the high cycle domain. The load history which the structure is subjected to, will be reduced to reversals using rainflow counting. Each of these reversals produces a multiaxial stress state in the structure, this state is transformed into an equivalent uniaxial amplitude stress with either the Sines criterion or signed von Mises where the mean stress effects are taken into account by using the modified Goodman equation. From this equivalent uniaxial amplitude stress, the number of cycles to failure is estimated using the Basquin curve. By employing Palmgren-Miners linear damage hypothesis a local damage constraint can be formulated, which like the yield constraint is handled by using an aggregate function.

These Topology optimization formulations are lastly solved for a number of standard benchmark examples in both 2D and 3D which illustrates the characteristics of fatigue constraints.

Resumé

Denne afhandling omhandler formuleringen og udførelsen af strukturel optimering ved brug af topologioptimering i både to og tre dimensioner, for storskala optimeringsproblemer hvori der indgår mange design variable. Topologioptimering stræber efter at finde den optimale fordeling af materiale indenfor et givet domæne, for en given kostfunktion og underlagt bestemte begrænsninger. Her er målet at minimere massen af en struktur, som er begrænset af flydespændings- og/eller udmattelsesbetingelser.

Første del af afhandlingen omhandler de generelle problemer som opstår når topologioptimering anvendes. Disse problemer som indeholder checkerboarding, netafhængige løsninger, minimum længde skala og sort/hvide strukturer, bliver illustrereret for den klassiske topologioptimerings formulering som omhandler minimering af fleksibiliteten underlagt en volumenbetingelse.

Både flydespændings- og udmattelsesbetingelser er afhængige af spændingerne som opstår i en struktur når den er underlagt en belastning. Derfor omhandler anden del de specifikke udfordringer som opstår når der inkluderes spændingbetingelser i topologioptimering. Først bliver selve formuleringen af spændingerne undersøgt når de indgår i densitetbaseret topologioptimering, derefter bliver det velkendte problem med singulære optima fremhævet. Det singulære optima problem bliver heri løst ved at anvende qp-metoden. På grund af den lokale natur af spændingsbetingelser, og siden denne afhandling betragter storskala optimeringsproblemer, bliver de associerede beregningsmæssige konsekvenser fremhævet og løst ved brug af en aggregatfunktion. På baggrund af det førnævnte kan en flydespændingsbegrænsning formuleres ved brug af von Mises flydespændings kriterie.

Foruden flydespændingsbetingelser formuleres også en betingelse baseret på udmattelse af strukturen. Udmattelse afhænger ligeledes af spændingerne i strukturen, derfor opstår mange af de samme problemstillinger som nævnt tidligere, og disse bliver løst med samme teknikker.

Udmattelsesbetingelsen bliver formuleret på baggrund af antagelser om proportional belastning med en variable amplitude samt en struktur med elastisk deformation i høj cyklusdomænet. Belastningshistorien som strukturen er udsat for bliver reduceret til belastningscyklusser ved brug af rainflow counting. Hver af disse cyklusser skaber en multiaksial spændingstilstand i strukturen, denne tilstand bliver transformeret til en ækvivalent uniaksial spændings amplitude ved brug af Sines kriteriet og signed von Mises hvor der bliver taget højde for middelspændingseffekterne ved at anvende den modificerede Goodman ligning. Fra en ækvivalent uniaksial spændingsamplitude estimeres antallet af cyklusser indtil brud ved brug af Basquin kurven, og ved at anvende Palmgren-Miners lineære skadeshypotese bliver der opstillet en lokal udmattelses betingelse, som ligeledes flydespændingsbetingelsen bliver håndteret ved brug af en aggregatfunktion.

Topologioptimering baseret på de opstillede betingelser bliver til sidst løst på en række standardproblemer i både 2D og 3D, som illustrerer de karakteristika der er ved udmattelsesbetingelser.

Table of contents

1 Introduction

This chapter will introduce the various aspects that concerns this thesis. Firstly the area of structural optimization with a specific focus on topology optimization will be addressed, then the motivation for including of yield and fatigue constraints is highlighted. Next, attention will be paid to the interest and importance of solving large-scale topology optimization problems. Lastly the objectives of the thesis will be outlined.

1.1 Structural Optimization

Structures in the following context are regarded as an assembly of material under the influence of loads, and optimization is the process of improvement, thus structural optimization can roughly be defined as finding the distribution of material which minimizes or maximizes a specific objective while being subjected to a set of constraints. This is done by using various modelling methods, such as displacement based linear finite element analysis as in the case of this thesis, to model the physics of the structure, and by employing mathematical optimization tools. The aim of using structural optimization is to increase the performance of the structure and reducing design time, when compared to conventional engineering design methods, which can be based on experience, intuition and heuristics. Generally structural optimization can be classified by three different approaches, size optimization, shape optimization and topology optimization, these are illustrated in figure 1.1

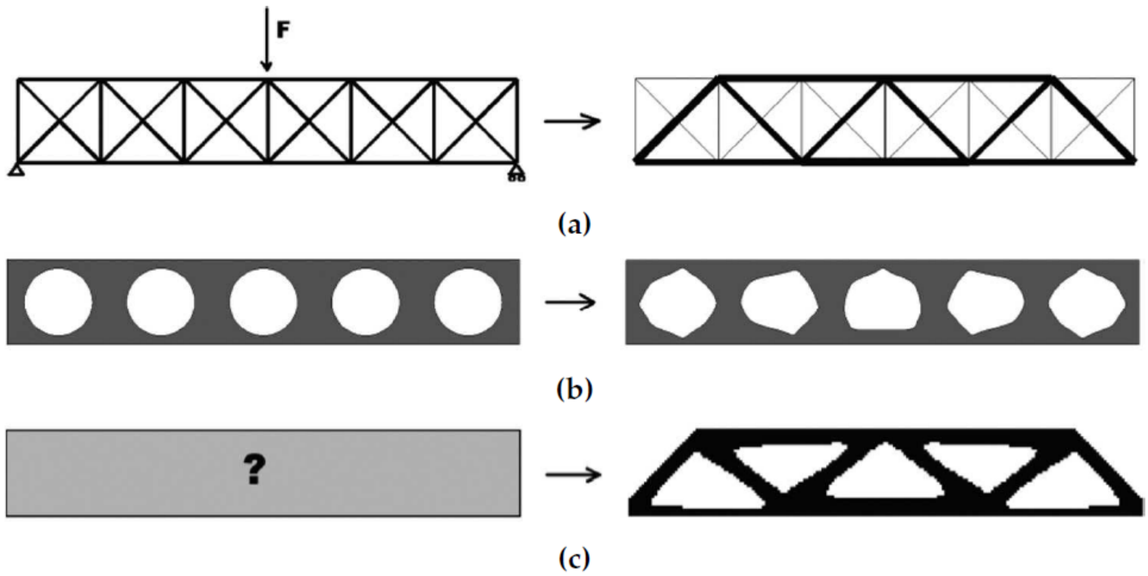

Figure 1.1: Structural optimization approaches (a) Size optimization, (b) Shape Optimization, (c) Topology Optimization (Bendsøe and Sigmund, 2003)

In size optimization the design variables are set to determine the size of a component in the structure, such as the cross sectional area of a truss as illustrated in figure 1.1, or the thickness of a plate and so forth. With shape optimization, the internal and or external boundary of a predetermined topological layout is modified. In both size and shape optimization, assumptions on the final structure is made from an initial design. In topology optimization no such assumptions are made, since it starts only from a predetermined design domain with load and boundary conditions applied. In this thesis topology optimization will be utilized.

Since the pioneering article by Bendsøe and Kikuchi (1988) topology optimization has greatly advanced as both a research field and in industrial application. Topology optimization problems have been formulated for a multitude of various physics, from its origin in structural mechanics to heat transfer, acoustics and dynamical response (Bendsøe and Sigmund, 2003). Numerous different optimization strategies have been established, approaching the topology optimization problem from different ways as illustrated in the review paper by Sigmund and Maute (2013). Various mathematical optimization methods have been applied, from gradient free zero-order methods to gradient based optimizers using first and or second order information. This thesis will be concerned with structural mechanics, considering a minimum mass objective while being subjected to yield and fatigue constraints. The topology optimization problem will be formulated using the density approach as proposed in Bendsøe (1989), and solved using first-order gradient based methods with the gradient information found using the adjoint method.

1.2 Yield & Fatigue Constraints

The industrial relevance of topology optimization have already been demonstrated, with its application in the aerospace industry as exemplified in Krog et al. (2002) where compliance minimization topology optimization was used in the early stages of a structural optimization procedure aiming to reduce the weight of the A380 leading edge droop nose ribs. Further examples include the optimization of a Porsche engine component (Matthias Penzel, 2015), where likewise compliance minimization was utilized.

The growing industry of additive manufacturing, exemplified by numerous projections and several companies commitment to the implementation of additive manufacturing, increases the need for new methods of engineering design. According to a collection of articles called "The great re-make: Manufacturing for modern times" published by McKinsey & Company (Blackwell et al., 2017) one of the two limitations presented with regards to the usage of additive manufacturing, was the lack of design knowledge -the other being design piracy-. It is presented, that at the present moment there is a considerable worldwide gap in the necessary knowledge in order to fully take advantage of additive manufacturing. A complete rework of the engineering design process is necessary, due to the added freedom that additive manufacturing provides, which allows for more organic structures not constrained by typical manufacturing methods, turning, milling, etc. While topology optimization certainly is no silver bullet, and the engineer must always be aware of accurate problem definition, adequate post processing and verification as well as the limitations of used topology optimization formulation. The unrestricted and automatized nature of topology optimization can provide the ability to utilize the manufacturing freedom of additive manufacturing. This is accomplished due to the limited number of assumptions on made the final design beforehand, while minimizing the necessity of the designers knowledge to generate optimal structures, which might be of complex and organic shape.

There are hurdles that must be overcome in order for topology optimization to be fully applicable within an industrial context. As illustrated in the design flow diagram 1.2, generally a design space is identified, then the optimization occurs, and based on the optimization results a production feasible design is attained.

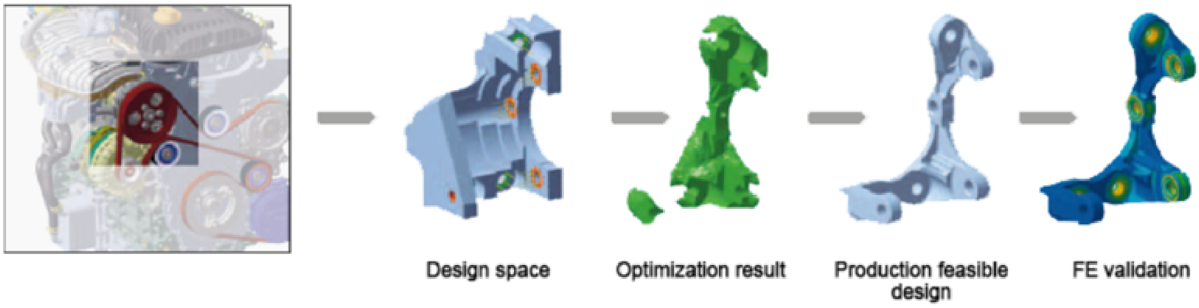

Figure 1.2: Design flow diagram of Porsche engine component (Matthias Penzel, 2015)

Often when considering a structural problem, failure of a component is of high priority. Thus, if using only compliance minimization with a volume constraint, a considerable amount post optimization effort might be necessary in order to obtain a structure which satisfies the necessary structural requirements. Thus, the inclusion of relevant failure constraints, such as yield stress and fatigue requirements, within the optimization formulation, would reduce the need for post optimization processing. The importance of considering failure due to fatigue is especially evident since 50% to 90% of all mechanical failures are estimated to be a result of fatigue failure (Stephens et al., 2001).

1.3 Large-Scale Optimization

In order to increase the applicability of topology optimization for industrial problems, the ability to perform large-scale 3D topology optimization is highly advantageous (Chin and Kennedy, 2016; Oest, 2017), since the increased resolution allows for the optimization of larger and more complex structures. Furthermore, as highlighted in the following articles (Aage et al., 2017) (Aage et al., 2015), can the increased resolution provide the ability to gain insight not available when using a coarser mesh. And as noted in Sigmund et al. (2016) a coarse mesh can put unintentional restrictions on the solution, resulting in a less optimized structure.

Considering the previous points the topology optimization problem in this thesis will implemented such that large scale 3D topology optimization can be performed. The implementations are made as extensions to the framework made available by the TopOpt group at DTU, which is made using the Portable and Extendable Toolkit for Scientific Computing (PETSc) (Aage et al., 2015). This framework allows for large scale optimization utilizing parallel computing, and has been demonstrated to solve problems with before unseen discretization levels.

1.4 Objectives

The main objective of this master thesis is to solve large scale 3D topology optimization problems with a minimum mass objective and subjected to yield and fatigue constraints. The yield constraints will be formulated using the von Mises yield criterion, while the fatigue constraints will be formulated assuming proportional loading with variable amplitude, and considering finite life under high cycle fatigue utilizing Palmgren-Miners damage rule, S—N curves and equivalent uniaxial amplitude criteria. The optimization will be performed using gradient based optimization with analytically determined gradients. The program will be verified on standard benchmark examples. The topology optimization procedure will be implemented using the PETSc framework, which allows for the solution of large scale problems in a reasonable amount of time, depending on the computational resources available.

Topology Optimization 2

As outlined in the introduction, topology optimization is concerned with finding the optimal distribution of material in a predefined domain for a given objective and subjected to a set of constraints. This chapter will introduce density based topology optimization, establish the material properties in terms of the design variables, formulate the classic minimum compliance topology optimization problem, and lastly illustrate the general issues that arises in topology optimization. It should be noted that all the optimization problem formulations are setup using the nested formulation, since the state problem is uniquely defined in terms of the design variables (Christensen and Klabring, 2009).

There exists multiple methods for solving a topology optimization problem, such as the level set approach, topological derivative and Phase field approach. However these methods will not be covered in this thesis, the method utilized here is the density approach which was first proposed in Bendsøe (1989).

Using this method a predefined domain is discretized using finite elements, as illustrated in figure 2.1 which shows a classic topology optimization benchmark example known as an MBB beam, which has a predefined height to length ratio of 1:6, with a force acting in the center and simply supported at lower corners. Here the domain is discretized using the linear elastic finite element formulation, using the linear Q4 plane elements in 2D and the linear 8 node brick element for 3D.

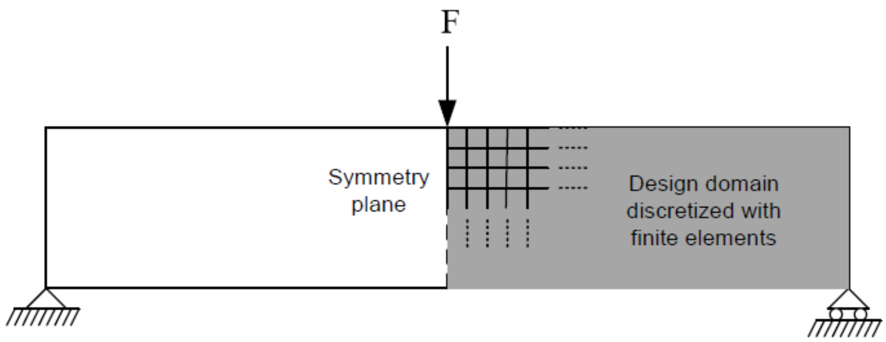

Figure 2.1: MBB beam (Oest, 2017)

Each of these elements are then assigned a dimensionless design variable ρ_e also referred to as the density variable. This density variable can be either 0 or 1, where 0 indicates void and 1 represent full material. The effective mass m_e and effective modulus of elasticity E_e of element e can then be described by multiplying the density variable with the full material equivalents m_0 and E_0.

$$E_e = \rho_e E_0$$
$$m_e = \rho_e m_0 \tag{2.1}$$
$$\rho_e = \{0, 1\}$$

Using the design variable as defined in equation 2.1 would result in a discrete optimization problem. However this thesis is concerned with large scale optimization problems with many design variables, and thus in order to efficiently solve the optimization problem gradient based methods are preferred, as highlighted in a forum article by Sigmund (2011) where gradient based methods are compared with non-gradient based methods. Therefore the discrete design variable is relaxed into a continuous design variable using the Solid Isotropic Material with Penalization method, abbreviated SIMP, as proposed in Bendsøe (1989).

In the SIMP method the discrete density variable is replaced with a continuous monotonically increasing function which is physically consistent at 0 and 1, such that 0 represents void material and 1 solid. When determining the effective modulus of elasticity, the intermediate density values are penalized using a power law approach, by raising the density variable to the power p which is called the penalization factor. Furthermore, in order to avoid getting singularities the modified SIMP method is utilized where a minimum modulus of elasticity $E_{min} = 10^{-6}E_0$ is introduced. Here the effective mass is linearly interpolated.

$$E_e = E_{min} + \rho_e^p(E_0 - E_{min})$$
$$m_e = \rho_e m_0 \tag{2.2}$$
$$\rho_e = [0, 1]$$

The effect of the penalization factor p on the effective modulus of elasticity is illustrated in figure 2.2 for various p values and a unit solid modulus of elasticity.

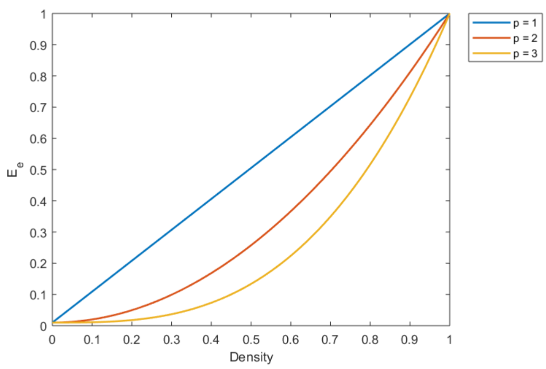

Figure 2.2: Effective Modulus for $p = 1, 2, 3$ for $E_0 = 1$

The value of the penalization factor p has a great influence on the convergence of the optimization procedure, a too low value minimizes the effect of penalization, and the result is a high number of intermediate density values, which is undesirable since generally a structure consisting mostly of a 0-1 distribution is preferred. A too high value of p results in premature convergence, based on numerical experiments $p = 3$ appears to give the best result (Bendsøe and Sigmund, 2003). This value was furthermore also shown to have physical meaning for $\nu = 0.3$ in Bendsøe and Sigmund (1999).

From these material parameters the governing equations can be determined as the following, with static or quasi-static loading assumed. Here boldface is used to indicate vector and matrices.

$$\boldsymbol{K}\boldsymbol{D} = \boldsymbol{R} \tag{2.3}$$

Here $\boldsymbol{K}$ is the global stiffness matrix, $\boldsymbol{R}$ is the load vector and $\boldsymbol{D}$ is the unknown displacement vector. The element nodal displacements $\boldsymbol{d}_e$ are extracted from the global displacement vector $\boldsymbol{D}$.

The global stiffness matrix is defined in terms of previous established material parameters, by using the finite element assembly operator on the individual element stiffness matrices $\boldsymbol{K}_e$, which are established by calculating the stiffness matrix for a unit modulus of elasticity $\boldsymbol{K}_0$, and multiplying with the effective modulus of elasticity as defined in (2.2).

$$\boldsymbol{K}_e = E_e \boldsymbol{K}_0 \tag{2.4}$$

$$\boldsymbol{K} = \sum_{e=1}^{n_e} \boldsymbol{K}_e \tag{2.5}$$

2.1 Compliance

Now that the material parameters have been defined in terms of the design variables, the compliance minimization problem can be established. Since its inception in Bendsøe and Kikuchi (1988) topology optimization has mostly been concerned with the maximizing the stiffness of a structure, which corresponds to minimizing the compliance of a structure. The minimum compliance problem thus aim to find the optimal distribution of material in order to achieve the highest stiffness of a structure while being subjected to a volume constraint. The optimization problem can be formulated as the following.

$$\begin{aligned} \underset{\rho}{\text{minimize}} \quad & f = \boldsymbol{D}^T \boldsymbol{K} \boldsymbol{D} = \sum_{e=1}^{n_e} \boldsymbol{d}_e^T E_e \boldsymbol{K}_0 \boldsymbol{d}_e \\ \text{subject to} \quad & g = \frac{\sum_{e=1}^{n_e} v_e \rho_e}{V^*} \leq 1 \\ & \rho_e = [0, 1] \end{aligned} \tag{2.6}$$

Here the objective function f is the compliance of the structure. The constraint g is the element volume v_e multiplied with the density variable summed over the number of elements in the domain n_e divided by the available amount of material defined by V^*.

2.1.1 Regularization

Solving the optimization problem as formulated in (2.6) illustrates some of the general issues that arises when performing topology optimization. These issues will here be demonstrated for a compliance minimization problem on the MBB benchmark example as illustrated in figure 2.1, however they are equally valid when considering a mass minimization objective, subjected to yield and or fatigue constraints. The first issue that will be highlighted is checkerboarding.

Checkerboarding as addressed in Díaz and Sigmund (1995) arises due to the use of linear elements in the discretization of the domain, which from the numerical modelling creates an artificially high stiffness for the alternating layout of void and solid elements as illustrated in figure 2.3

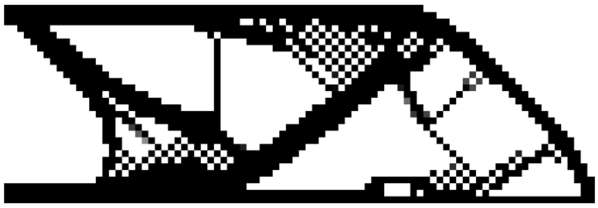

Figure 2.3: Checkerboarding MBB

This effect is highly undesirable since it is a product of numerical modelling, and does therefore not represent the physics correctly. The second issue is that of mesh dependent solutions. As the continuum formulation of the optimization problem is discretized into finite elements the solution becomes dependent on the degree of mesh refinement. As the mesh refinement increases the solution does not converge to a specific topological layout, rather as illustrated in figure 2.4 more detailed structures appear. This occurs due to the fact that the topology optimization problem as formulated in (2.6) lacks a general solution and is thus an ill-posed problem (Bendsøe and Sigmund, 2003).

Figure 2.4: Illustration of mesh dependency and minimum length scale with mesh refinement

Referring to figure 2.4 it can also be seen, that as mesh refinement increases, smaller details in the structure occurs and from a manufacturing point view the ability to set a minimum length scale on the final structure is advantageous. Numerous methods have been proposed for solving each of the highlighted issues, for a review of the possible methods refer to Bendsøe and Sigmund (2003) and Sigmund and Petersson (1998).

The method utilized in this thesis is the use of filtering techniques, specifically the density filter as first proposed in Bourdin (2001) and Bruns and Tortorelli (2001), for more information regarding general filtering techniques refer to Sigmund (2007). The density filter works by limiting the degree of density variation between elements, by making the density of an element e the weighted average of all elements within a circle in 2D or sphere in 3D of influence as determined by the following equation.

$$\omega_j = r_{filter} - \parallel \boldsymbol{x}_j - \boldsymbol{x}_e \parallel \quad if \parallel \boldsymbol{x}_j - \boldsymbol{x}_e \parallel \leq r_{filter} \tag{2.7}$$

Here ω_j is the weight function used to determine the filtered density value of element e, r_{filter} is a predetermined mesh independent filter radius that determines the size of the sphere of influence, as illustrated in figure 2.5. The weight function here is linearly decaying as distance between element e and j determined by their respective coordinates $\boldsymbol{x}_e$ and $\boldsymbol{x}_j$, increase.

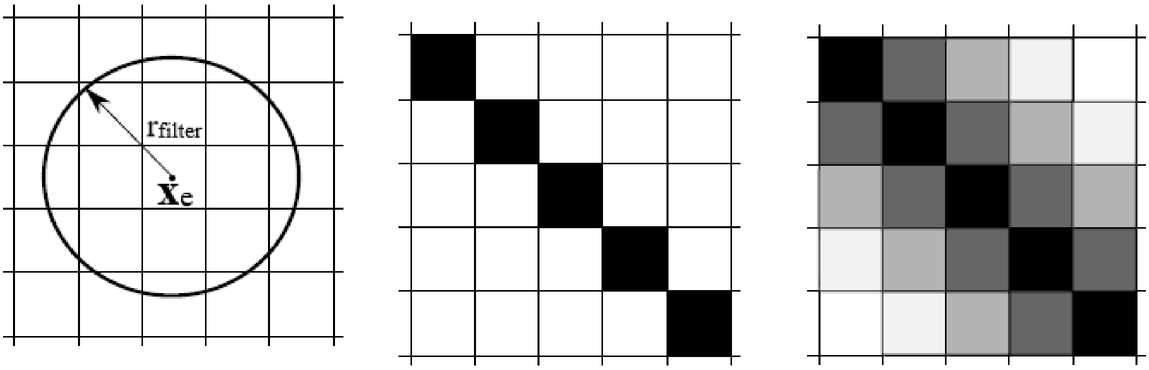

(a) Filter radius and coordinates of element e

(b) Design variables

(c) Filtered Density

Figure 2.5: llustration of the effect of the density filter on an arbitrary design variable distribution. (Oest, 2017)

This is done within the distance of the filter radius, beyond the filter radius the weight factor is 0. The filtered density $\tilde{\rho}_e$ is found by a weighted average equation

$$\tilde{\rho}_e = \frac{\sum_{j=1}^{n_e} \omega_j \rho_j}{\sum_{j=1}^{n_e} \omega_j} \tag{2.8}$$

2.1.2 Projection Filter

Using the density filter inevitably introduces a transition zone, between the solid and void parts of the structure of intermediate density values as seen in figure 2.5c. Since intermediate densities have no physical relevance it is desirable to achieve a final structure consisting mainly of solid and void densities. In Guest et al. (2004) a solution was proposed by modifying the density filter by including a continuous approximation of the Heaviside function, which would force all intermediate densities greater than 0 to 1, thereby creating void and solid structures. Modifications to this general idea has been proposed in Sigmund (2007) where the modified Heaviside filter was introduced which opposite the standard Heaviside filter, force all intermediate densities below 1 to 0. In Xu et al. (2010) the threshold filter is established, here a threshold value η is introduced where all densities below or equal to this value are projected to 0, and all above are projected to 1 as formulated in (2.9).

$$\tilde{\rho}_e = \begin{cases} 0 & \text{if } \tilde{\rho}_e^* \leq \eta \\ 1 & \text{otherwise} \end{cases} \tag{2.9}$$

Here $\tilde{\rho}_e^*$ indicates the density value obtained after using the density filter (2.8). The condition above is approximated using the following continuous and differentiable equation (2.10) put forth by Wang et al. (2011), where β determines the degree of the threshold filter approximation (2.9), as illustrated in figure 2.6, where it can be seen that the larger the β values, the closer the approximation. The β value is gradually increased during the optimization using a continuation scheme from a low value to an appropriately high value until the desired level of density discreteness is accomplished.

$$\tilde{\rho}_e = \frac{tanh\left(\beta\eta\right) + tanh\left(\beta\left(\tilde{\rho}_e^* - \eta\right)\right)}{tanh\left(\beta\eta\right) + tanh\left(\beta\left(1-\eta\right)\right)} \tag{2.10}$$

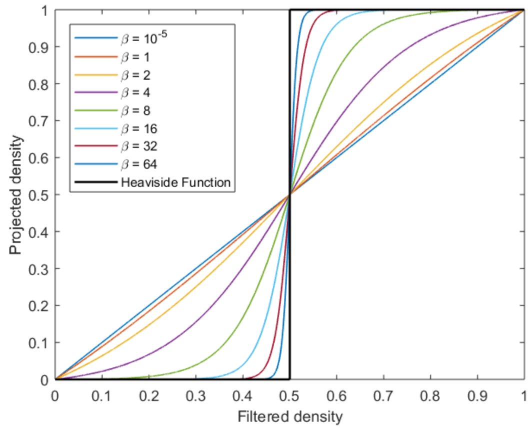

Figure 2.6: Effect of $\beta = 10^{-5} \rightarrow 64$ on projected density at $\eta = 0.5$

Using the threshold filter given by (2.10) as opposed to the Heaviside and modified Heaviside filters offers additional advantages. By introducing the threshold value, some of the numerical instabilities which occur by using the Heaviside filters with stress based constraints, can be reduced by setting η away from either extreme of 0 and 1, and closer to 0.5. Furthermore, by selecting appropriate filter radius and η value, provides the ability to set a minimum length scale on both the solid and void parts of the structure, which is advantages from a manufacturing perspective. Figure 2.7 illustrates the transition zone of the density filter, and the effect of applying the threshold filter.

Figure 2.7: Effect of threshold filter for V*=0.4 of the original domain, $n_e = 10800$, filter radius = 6 elements, $\eta = 0.5$, $\beta = 32$

Henceforth the filtered density is referred to as the physical density since this density now represents the structure, and both the objective function and constraints are evaluated based on these densities. The minimum compliance optimization problem is now formulated in terms of the physical densities as the following.

$$\begin{aligned} \underset{\rho}{\text{minimize}} \quad & f = \boldsymbol{D}^T \boldsymbol{K} \boldsymbol{D} = \sum_{e=1}^{n_e} \boldsymbol{d}_e^T E_e \boldsymbol{K}_0 \boldsymbol{d}_e \\ \text{subject to} \quad & g = \frac{\sum_{e=1}^{n_e} v_e \tilde{\rho}_e}{V^*} \leq 1 \\ & \rho_e = [0, 1] \end{aligned} \tag{2.11}$$

Stress Constraint 3

Weight reduction of structures is an aim across various industries at practically any scale and offers numerous benefits, such as lower fuel consumption, performance gain and a reduction in material cost. However weight reduction is constrained by several mechanical failure modes. Many of these failure modes are dependent on the stresses that occur in a structure when it is subjected to loading, more specifically the failure mode which is considered in the following chapter is yielding. Yielding occurs when the deformation of the material transition from elastic to plastic, the point at which this occurs is defined by the yield stress limit σ_{lim}. There exists numerous yield criteria, however the most commonly used for ductile materials is the von Mises yield criterion, which states that yielding occurs when the von Mises stress σ_{vm} equals the yield stress limit σ_{lim}. Furthermore, the yielding constraint is necessary to enforce the assumption of linear elasticity. Here the von Mises stress is calculated for each element by the following equation.

$$\sigma_{vm\,e} = \frac{1}{\sqrt{2}}\sqrt{(\sigma_{e_1} - \sigma_{e_2})^2 + (\sigma_{e_2} - \sigma_{e_3})^2 + (\sigma_{e_3} - \sigma_{e_1})^2 + 6(\sigma_{e_4}^2 + \sigma_{e_5}^2 + \sigma_{e_6}^2)} \tag{3.1}$$

In (3.1) σ_{e_1} - σ_{e_6} are the stress components for element e in 3D.

This then establishes a constraint for each element in the domain, where the von Mises stress (3.1) must below the yield stress limit σ_{lim}. The optimization problem can now be formulated with the objective being minimizing the mass, and subjected to the von Mises constraint for each element. Here we assume constant material density such that minimizing the mass corresponds to minimizing the volume, furthermore, the domain volume V_0 is introduced such that the objective function is normalized.

$$\begin{aligned} \underset{\rho}{\text{minimize}} \quad & f = \frac{1}{V_0}\sum_{e=1}^{n_e} v_e \tilde{\rho}_e \\ \text{subject to} \quad & g_e = \left(\frac{\sigma_{vm\,e}}{\sigma_{lim}}\right) \leq 1 \quad \forall e \\ & \rho_e = [0, 1] \end{aligned} \tag{3.2}$$

Including stress constraints within the topology optimization formulation introduces new complications not present when considering the minimum compliance problem. When considering the minimum compliance problem subjected to a volume constraint, both the objective function and the constraint are global functions, compare that to the stress constraint which is a local quantity. This greatly increases the computational effort necessary to solve the problem, as the number of constraints equals the number of elements within the domain. Furthermore, the singular optima problem that arises from stress constraints, as first noted in Sved and Ginos (1968), requires special consideration if the optimization problem is to be solved adequately. These two issues will be elaborated upon further on, however due to the use of the SIMP method a stress interpretation when considering intermediate densities has be to established.

3.1 Stress Formulation

If the topology optimization problem was formulated as a discrete optimization problem with the density variable being either 0 or 1, the stress would be either full stress for a solid material or zero stress for void material. However due the relaxation of the discrete problem into a continuous problem a stress criterion for an intermediate density is necessary. A stress criterion could be based on the effective modulus of elasticity formulated as the following.

$$\boldsymbol{\sigma}_e = \boldsymbol{C}(E_e)\boldsymbol{\epsilon}_e \tag{3.3}$$

Where $\boldsymbol{\sigma}_e$ is the element stress vector in Voigt notation.

$$\boldsymbol{\sigma}_e = \{\sigma_{e1}\,\sigma_{e2}\,\sigma_{e3}\,\sigma_{e4}\,\sigma_{e5}\,\sigma_{e6}\}^T \tag{3.4}$$

$\boldsymbol{C}(E_e)$ is the constitutive matrix (Dym and Shames, 2013) as a function of the effective modulus of elasticity and $\boldsymbol{\epsilon}_e$ is the element strain vector defined as.

$$\boldsymbol{\epsilon}_e = \boldsymbol{B}\boldsymbol{d}_e \tag{3.5}$$

Here $\boldsymbol{B}$ is the strain-displacement vector which for 2D and 3D can be found in Cook et al. (2001). However, this stress criterion is not appropriate since it generally will lead to an all void design (Verbart, 2015). This is due to the fact that the strains are proportional to $\tilde{\rho}_e{}^{-p}$ while the effective modulus of elasticity is proportional to $\tilde{\rho}_e^p$, thus the stress becomes invariant to the density.

Duysinx and Bendsøe (1998) proposed another physically consistent stress formulation based on the study of rank-2 composite materials, the stress formulation was based on the following requirements. Firstly, the stress must be inversely proportional to the density value, this can formulated as the following, where the constitutive matrix now is a function of the solid modulus of elasticity, and q is an arbitrary exponent.

$$\boldsymbol{\sigma}_e = \frac{\tilde{\rho}_e^p}{\tilde{\rho}_e^q}\boldsymbol{C}(E_0)\boldsymbol{\epsilon}_e = \tilde{\rho}_e^{p-q}\boldsymbol{C}(E_0)\boldsymbol{\epsilon}_e \tag{3.6}$$

Furthermore, in order to remain coherent with the stress criterion for a rank-2 composite, the stress must converge to a finite and non zero stress as the density goes to zero for finite strain. The condition which satisfies this coherence requirement is for $q = p$, and thus the stress criterion can be stated as.

$$\boldsymbol{\sigma}_e = \boldsymbol{C}(E_0)\boldsymbol{\epsilon}_e \tag{3.7}$$

3.2 Singular Optima

As noted previously, the problem of singular optima when considering stress constraints have been known since it was highlighted in Sved and Ginos (1968), where a three-bar truss system was analysed and it was found that the true optima of a two-bar solution was unattainable with gradient based methods due to the presence of the stress constraints. It was later explained that the issue arises due to the discontinuity of the stress constraint, since the stress tends toward a finite value as the density go towards zero, while being zero for zero density. This discontinuity generates degenerate subspaces in the feasible domain, that are inaccessible to standard optimization methods. Within the context of topology optimization this means that the coherence requirement as stated in the section above, which requires the convergence to a finite stress as the density goes towards zero, might cause stresses that violate the yield constraint, thus inhibiting material removal due to the constraint violation. Furthermore, as noted in Bruggi (2008) the box constraint imposed in the density variable can make the subspaces generated by the stress discontinuity not only degenerate, but also disjointed from the feasible domain.

Several methods have been proposed to solve this problem, the two most well known being the ϵ-relaxation method (Cheng and Xu, 1997) where a relaxation ϵ is introduced which perturbs the feasible domain, and makes the global optima available, the ϵ parameter is then gradually decreased, whereby the relaxed problem approaches the original formulation. The second method is the qp-approach, first illustrated in Duysinx and Bendsøe (1998) and elaborated upon further in Bruggi (2008) and Le et al. (2010), the qp-approach is the method that will be used in this thesis. In the qp-approach the global optima is made available by relaxing the coherence requirement which stated the following.

$$\boldsymbol{\sigma}_e = \lim_{\tilde{\rho}_e \to 0} \tilde{\rho}_e^{p-q} \boldsymbol{C}(E_0) \boldsymbol{\epsilon}_e = \boldsymbol{C}(E_0) \boldsymbol{\epsilon}_e \quad for \quad q = p \tag{3.8}$$

Now, by replacing the $q = p$ requirement, with $q < p$ the stress will converge to a zero stress as the density goes towards zero.

$$\boldsymbol{\sigma}_e = \lim_{\tilde{\rho}_e \to 0} \tilde{\rho}_e^{p-q} \boldsymbol{C}(E_0) \boldsymbol{\epsilon}_e = \mathbf{0} \quad for \quad q < p \tag{3.9}$$

Thus, the physical consistency for intermediate densities as determined from the study of rank-2 composites, is sacrificed for a stress definition which makes the global optima available, by making the constraint consistent for 0 and 1 densities. The stress formulation can thus be stated as the following, where $qp = p - q$.

$$\boldsymbol{\sigma}_e = \tilde{\rho}_e^{qp} \boldsymbol{C}(E_0) \boldsymbol{\epsilon}_e \tag{3.10}$$

As noted in Le et al. (2010) this is effectively a stress penalization, where low densities produce higher stresses as illustrated in the following figure.

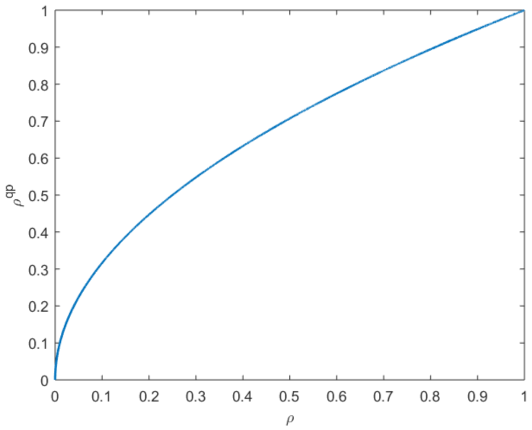

Figure 3.1: Effect of qp-relaxation on density variable for qp = 0.5

From figure 3.1 it is also visible that as the density approaches zero, the gradient becomes infinite. This motivates the introduction of a minimum density value ρ_{min}. Based on numerical experiments and recommendations by Collet et al. (2017) it was found that minimum density in range of 10^{-3} - 10^{-5} did not effect the optimization problem, thus henceforth $\rho_{min} = 10^{-5}$ is set for the optimization problem formulation containing the stress formulation (3.10).

3.3 Local Constraints

The second issue that arises when considering stress based constraints is the local state of the stress. Generally within topology optimization the stresses are evaluated in the center of each element, corresponding to the superconvergent point for linear elements, which is where the stresses, especially the shear stresses, are the most accurate. The result of this, is that the number of constraints equals the number of design variables. Due to this local state, the computational effort for solving large problems when considering local stress constraint becomes inefficient. Especially when considering that the optimization problem is to be solved using gradient based methods, which if local stress constraints were to be considered, would require the sensitivity of each constraint with respect the each design variable was to be found, this would greatly increase the computational resources necessary for solving the problem.

Various methods have been proposed in order to reduce the expensive computation associated with local stress constraints. The method utilized in this thesis is the use of aggregate functions. By using an aggregate function the local stress constraints are converted into a global constraint that represents the maximum von Mises stress in the domain, while still being first order differentiable. There are multiple examples of different aggregation functions being used, each having a various characteristics. For example, Kreisselmeier Steinhauser (KS) aggregation as used in Verbart (2015) provides the ability to have negative input variables. Here the input values are all positive, therefore is the aggregate function applied here is the P-norm function (3.11) denoted as Ψ.

$$\Psi = \left(\sum_{i=1}^{n_e} \sigma_{vm\,i}^{P} \right)^{\frac{1}{P}} \tag{3.11}$$

The P-norm aggregate function Ψ takes as input the local von Mises stress for each element, and an aggregate parameter $P > 0$. The P parameter determines the accuracy of the aggregate functions approximation of the maximum value, and in the limit as P goes towards infinity the P-norm function equals the maximum stress.

$$\lim_{P \to \infty} \Psi(\boldsymbol{\sigma}_{vm}, P) = max(\boldsymbol{\sigma}_{vm}) \tag{3.12}$$

The P-norm aggregate function is illustrated in figure 3.2 for different P values, where it approximates the maximum function value at x of two different functions illustrated by the broken black lines.

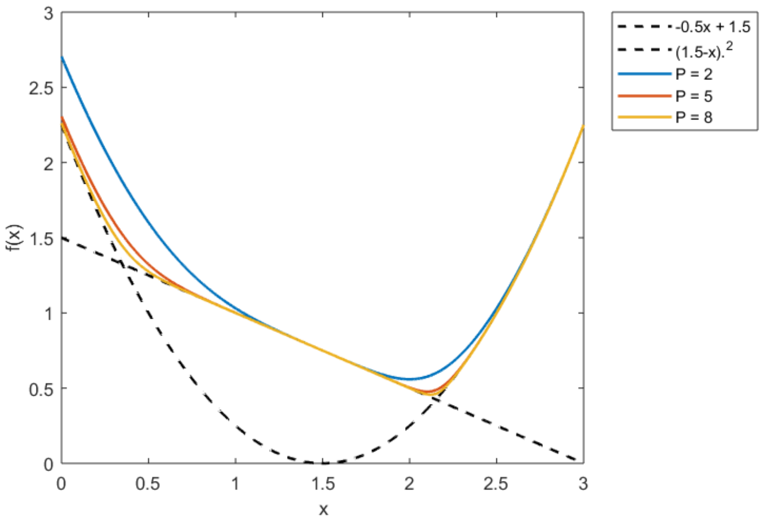

Figure 3.2: P norm approximation for P = 2,5,8

As can be seen in figure 3.2 as the P value increase, so does the accuracy of maximum value approximation. Furthermore, it is also illustrated that the P-norm aggregate function approaches the maximum value from above, such that when using the P-norm function the maximum value is overestimated leading to a more conservative structure since constraint is based on the approximated maximum value.

The accuracy of the aggregate function is also dependent on the number of input values, such that an increase in input values decreases the accuracy of the maximum value approximation. Considering large optimization is the goal of this thesis, a P value larger than generally applied in the literature might be required due to increased number of input values. In order to achieve a good approximation a high P value is necessary, however the higher the P value the more non-linear the optimization problem becomes. A high P value will decrease the speed of convergence, or even completely inhibit convergence.

The specific value of the P parameter is problem dependent and is determined from numerical experiments guided by recommendations in the literature. Depending on the problem to be solved, a P value in the range of 6-16 appears to be a good compromise between the aspects of convergence and sufficient representability. These P values presuppose a combination with the adaptive constraint scaling factor as described in the next section.

3.4 Adaptive Constraint Scaling

As remarked in the previous section, the aspects of convergence is highly dependent on the degree of non-linearity of the optimization problem, which motivates the use of a low P value, however this introduces the issue of overestimation. The issue of overestimation by the P-norm aggregate function is mitigated by a method proposed in Le et al. (2010) known as adaptive constraint scaling. The general idea is to minimize the discrepancy between the approximated value and the real maximum value by introducing a scaling factor c at the current iteration I which scales the aggregate value Ψ.

$$max(\boldsymbol{\sigma}_{vm}) \approx c^{(I)}\Psi \tag{3.13}$$

This scaling factor is then determined using information of the maximum von Mises stress and the aggregate value from the previous iteration $(I-1)$.

$$c^{(I)} = \alpha^{(I)} \frac{max(\boldsymbol{\sigma}_{vm})^{(I-1)}}{\Psi^{(I-1)}} + \left(1-\alpha^{(I)}\right) c^{(I-1)} \tag{3.14}$$

$$\alpha^{(I)} = (0, 1] \tag{3.15}$$

Here α serves as a dampening factor, which becomes active if c oscillates between two consecutive iterations. This method makes it possible to adequately solve the problem with a lower P value. The c factor is dependent on the $max()$ function, which makes it non differentiable, and is therefore not included in the sensitivity analysis. However, as noted in Le et al. (2010) as the optimization converges the difference between the c factors becomes smaller, and thus reducing the influence of the non-differentiability. The adaptive constraint scaling method is implemented as illustrated in the following pseudo code from Oest and Lund (2017b).

Algorithm 1 Pseudo Code - Adaptive Constraint Scaling Method

if $I \leq 2$ **then**
  $c^{(I)} = \frac{max(\boldsymbol{\sigma}_{vm})^{(I)}}{\Psi^{(I)}}$
  $\alpha^{(I)} = 1$
else
  if *Oscillation* **then**
    $\alpha^{(I)} = max(0.5, \alpha^{(I-1)}0.8)$
  else
    $\alpha^{(I)} = min(1, \alpha^{(I-1)}1.2)$
  end if
  $c^{(I)} = \alpha^{(I)} \frac{max(\boldsymbol{\sigma}_{vm})^{(I-1)}}{\Psi^{(I-1)}} + \left(1-\alpha^{(I)}\right) c^{(I-1)}$
end if

The optimization problem considering mass minimization while being subjected the von Mises stress constraints can now be formulated, utilizing qp relaxation to handle the issue of singular optima, and a scaled aggregate function to increase the computational efficiency.

$$\begin{aligned} \underset{\rho}{\text{minimize}} \quad & f = \frac{1}{V_0} \sum_{e=1}^{n_e} v_e \tilde{\rho}_e \\ \text{subject to} \quad & g = \left(\frac{c^{(I)} \Psi}{\sigma_{lim}} \right) \leq 1 \\ & \rho_e = [\rho_{min}, 1] \end{aligned} \tag{3.16}$$

Fatigue Analysis 4

The inclusion of fatigue constraints within topology optimization is relatively recent. In Holmberg et al. (2014) and Holmberg (2016) the topology optimization and fatigue analysis were done separately, where the fatigue analysis determined an equivalent fatigue life stress constraint. This equivalent stress would then be used as a constraint in combination with a von Mises constraint in the topology optimization problem. In Jeong et al. (2015) a fatigue constraint was considered with mean stress effects and for constant loading conditions. Fatigue constrained topology optimization has also been performed in the frequency domain as opposed to the time domain Lee et al. (2015). In Oest and Lund (2017b) the fatigue analysis, considering variable amplitude loading in the time domain, was included in the topology optimization problem, and efficiently solved using gradient based methods, where the sensitivities were found using the adjoint method.

The often cited statistic, that failures due to fatigue account for 50% to 90% of all mechanical failures (Stephens et al., 2001), illustrates both the prevalence of mechanical structures which are subjected to repeated loading, as well as the difficulty of designing a component for fatigue. Adequately designing a component for fatigue requires numerous inputs, such as geometry, load history, material data and environmental effects, the accuracy of which can have a great impact on the final prediction.

The designer must furthermore choose an appropriate fatigue life model. Generally there exists four different models, namely the nominal stress life method (S-N), the strain life method (ϵ - N), the fatigue crack growth model and lastly the two stage model which is a combination of the strain life method and the fatigue crack growth model. Each of these models have their area of best applicability, the S-N method is most appropriate for high cycle fatigue, which is generally characterised by elastic strains, and generally determined as being when the number of cycles are greater than 10^3 (Norton, 2011). The ϵ-N method has the best correlation with experiments when considering low cycle fatigue, and in areas where plastic deformation occurs, such that accounting for the loading in terms of strains opposed to stresses offers a simpler and more accurate description. If knowledge of a crack in the structure exists, then the fatigue crack growth model provide the ability the predict the life time. The two stage model utilizes the ϵ-N method to estimate the crack initiation and subsequently the fatigue crack growth model. In this thesis, the concern is of structures which are subjected to high cycle fatigue, and also is subjected to a yield constraint such that only elastic strains occur, thus the S-N method is the most suitable.

After an appropriate fatigue life model has been chosen, numerous methods are available for estimating the fatigue life. The method has to be selected based on various conditions, such as whether an uniaxial and multiaxial stress state occurs, variable or constant amplitude loading, design for infinite or finite life time and the available computational resources. The structures considered here are in a multiaxial stress state, which for high cycle fatigue generally are analysed using two methods, the equivalent uniaxial amplitude stress method, and critical plane analysis. Using critical plane analysis, a plane which is at the highest risk of failure is determined at a given stress state. As highlighted in (Svärd, 2015a), determining this critical plane is computationally expensive, since the problem of finding this critical plane is generally non-concave and thus using gradient based methods might not find the critical plane, in light of this, the brute-force method is generally utilized. Therefore, since large scale optimization is considered here, this method is not applicable with the computational resources available. The other conditions necessary to establish a fatigue constraint will be examined and elaborated upon in the following sections.

This chapter will outline the individual components necessary to define the fatigue constraints utilized in the topology optimization. Initially the loading conditions and the decomposition of these into load reversals will be considered. Then an uniaxial equivalent amplitude stress is established from the multiaxial stress state, which includes the mean stress effects. Lastly the damage that occurs over a set lifetime is estimated considering high cycle fatigue, using S-N curves and the accumulated damage method.

4.1 Loading Conditions

The following section describes the loading conditions considered in this thesis, as well as the method used to reduce the load history into load reversals.

4.1.1 Proportional Loading

When performing a fatigue analysis, it is important to identify the loading condition that the structure is subjected to, since some fatigue analysis tools are limited to a specific case, and thus applying non suitable fatigue assessment method might result in an erroneous prediction. There exist two classifications, namely proportional loading and non-proportional loading, these will be illustrated with the following example of a shaft subjected to axial and torsional loading as illustrated in figure 4.1a.

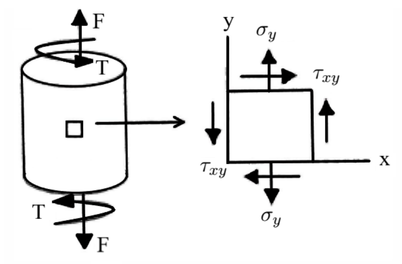

(a) Shaft subjected to axial and torsional loading

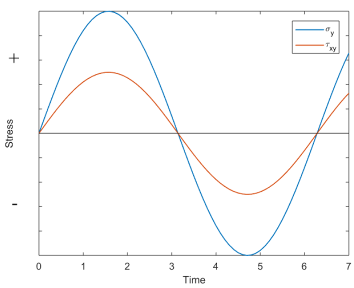

(b) Proportional loading

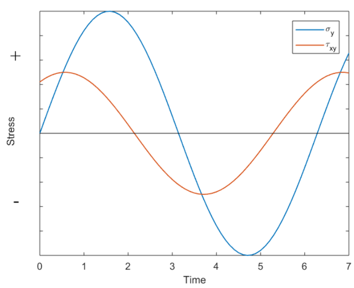

(c) Non-proportional loading

Figure 4.1: Loading example (Stephens et al., 2001)

If the axial and torsional load is applied in sync, it would result in the stress state in 4.1b where the proportion between the normal and shear stress is always equal, hence the name proportional loading. However, if the loads are applied out of phase, the stress state 4.1c occurs.

In this thesis proportional loading is assumed, this allows for the use of equivalent stress based approaches, and the possibility to apply cycle counting methods on the load-time history, rather than on the stress-time history for each element which possibly could be computationally expensive.

4.1.2 Cyclic Loading

Many of the structures where fatigue is relevant are subjected to variable amplitude loading, therefore, and for the sake of generality so to are the structures considered in this thesis. The nomenclature related to fatigue, is introduced in figure 4.2 which illustrates a constant amplitude loading for uni-axial stress.

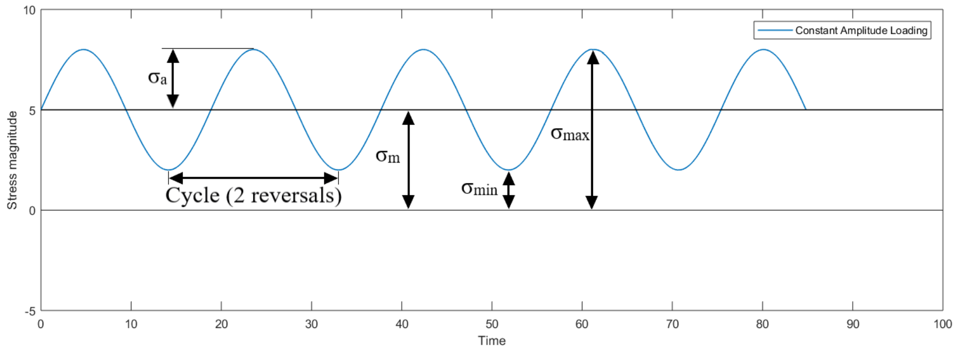

Figure 4.2: Constant amplitude loading

Here the stress amplitude σ_a and the mean stress σ_m is calculated from the following equations

$$\sigma_a = \frac{(\sigma_{max} - \sigma_{min})}{2} \tag{4.1}$$

$$\sigma_m = \frac{(\sigma_{max} + \sigma_{min})}{2} \tag{4.2}$$

Figure 4.2 illustrates the load history for constant amplitude cyclic loading, however the variable amplitude loading considered here would resemble the load history illustrated in figures 4.3 and 4.4.

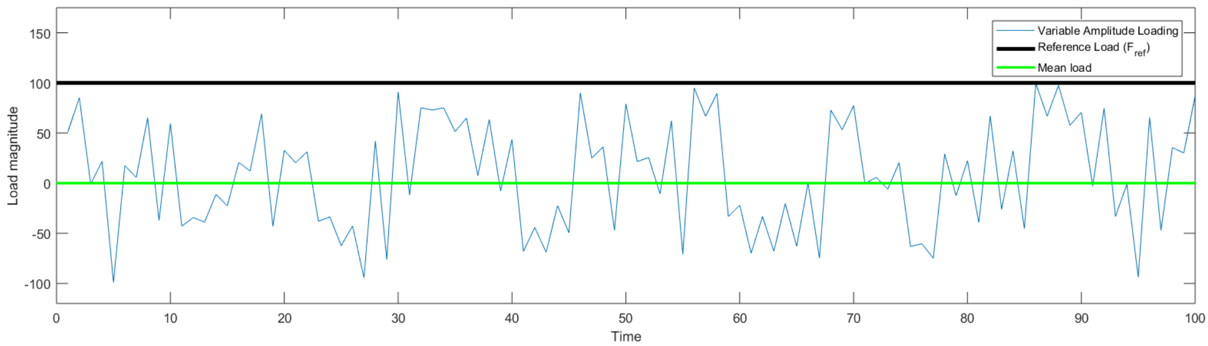

Figure 4.3: Variable amplitude load history for F_{ref} = 100 and r = -1

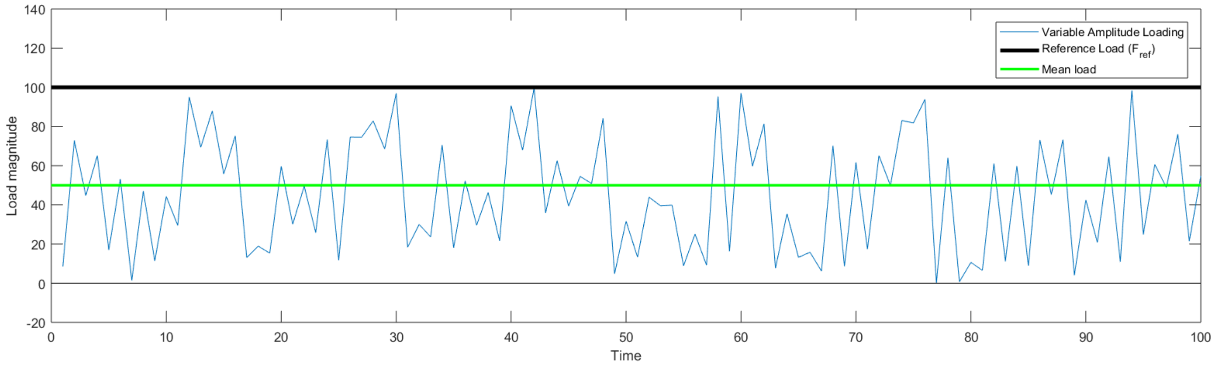

Figure 4.4: Variable amplitude load history for F_{ref} = 100 and r = 0

The load histories illustrated in figures 4.3 and 4.4 are randomly generated based on a specified load ratio referred to as r, and a reference load F_{ref}. Where the r ratio is the ratio between the maximum or reference load and the minimum load.

$$r = \frac{F_{min}}{F_{ref}} \tag{4.3}$$

The two illustrated load histories are for the two most common load ratios, namely fully reversed loading shown in figure 4.3 where the load varies within an interval between a equal valued positive and negative reference load, with a mean load of 0 corresponding to r=-1. Figure 4.4 illustrates what is called fluctuating or pulsating load where r=0. Here the load varies between 0 and the reference load with a mean of half the reference load.

4.1.3 Rainflow Counting

In order to account for the damage of a given load history, this history has to be decomposed into load reversals. This is done by applying a cycle counting method to a representative section of the complete load history. This gives the amplitude and mean values of a given load reversal, as well as the number of load reversals. There are numerous counting methods available, here rainflow counting is used since it is the most popular and probably the best counting method (Stephens et al., 2001).

The rainflow counting method was proposed in 1968 by T. Endo and M. Matsuishi. Here, the load-time history plot is reduced to peaks and valleys. From these peaks and valleys, the amplitude and mean scaling factors of the individual load reversals as well as the number of load reversals can be found by applying a specific counting method outlined in (Stephens et al., 2001). The amplitude and mean scaling factors c_a, c_m are found from the relationship between a reference load F_{ref} and the amplitude and mean load of the load reversal, such that there is a scaling factor for each rainflow as indicated by the index i.

The reference load illustrated in figure 4.3 and 4.4 is used in the equilibrium equations (2.3), which yields the reference displacements. From these reference displacements, element reference stresses can be found for each element (3.10). Since linear elasticity is considered the principle of superposition can be utilized, such that the mean and amplitude stress components for each element and each load reversal can be found from the element reference stress vector and the scaling factors.

$$\boldsymbol{\sigma}_{e_{a,i}} = c_{a,i}\boldsymbol{\sigma}_e \tag{4.4}$$

$$\boldsymbol{\sigma}_{e_{m,i}} = c_{m,i}\boldsymbol{\sigma}_e \tag{4.5}$$

4.2 Equivalent Stress

Since the structure is subjected to a 3D multiaxial stress state and we would like to use the data available from uniaxial stress tests in the form of S-N curves, the 6 stress components have to be combined into a equivalent uniaxial amplitude stress. In this thesis two equivalent stress criteria are considered, namely Sines criterion as considered in Oest and Lund (2017b) and signed von Mises with mean stress effects presented in Stephens et al. (2001) and Jeong et al. (2015). The motivation for introducing the signed von Mises equivalent stress, is based on a correspondence with Grundfos, which utilizes the signed von Mises criteria in order to design and validate some of their components.

4.2.1 Sines criterion

Sines proposed using the octahedral shear stress for the amplitude stress, and the hydrostatic stress for the mean stress. These two terms are then added to produce an equivalent uniaxial amplitude stress.

$$\tilde{\sigma}_{sines,a_e} = \frac{1}{\sqrt{2}}\sqrt{(\sigma_{1_e} - \sigma_{2_e})^2 + (\sigma_{2_e} - \sigma_{3_e})^2 + (\sigma_{3_e} - \sigma_{1_e})^2 + 6(\sigma_{4_e}^2 + \sigma_{5_e}^2 + \sigma_{6_e}^2)} \tag{4.6}$$

$$\tilde{\sigma}_{sines,m_e} = \frac{1}{\sqrt{2}}\beta(\sigma_{1_e} + \sigma_{2_e} + \sigma_{3_e}) \tag{4.7}$$

The equivalent amplitude $\tilde{\sigma}_{sines,a_e}$ and equivalent mean stress $\tilde{\sigma}_{sines,m_e}$ are calculated based on the reference stress, and then scaled using load scaling factors c_a and c_m to determine an equivalent uniaxial amplitude stress $\tilde{\sigma}_{e_i}$ for each element and rainflow, indicated by their respective subscript e and i.

$$\tilde{\sigma}_{sines\,e_i} = c_{a_i}\tilde{\sigma}_{sines,a_e} + c_{m_i}\tilde{\sigma}_{sines,m_e} \tag{4.8}$$

Here β is a material parameter of mean stress influence, which in the absence of experimental data can be set to $\beta = 0.5$ (Stephens et al., 2001). A negative Sines equivalent stress is assumed to cause no damage (Oest and Lund, 2017b).

4.2.2 Signed von Mises

Using the signed von Mises equivalent stress, an equivalent amplitude $\sigma_{vm,a_{e_i}}$ and an equivalent mean stress $\sigma_{vm,m_{e_i}}$ is determined from multiplying the amplitude and absolute mean scaling factors with the element reference von Mises stress σ_{vm_e} (Stephens et al., 2001).

$$\sigma_{vm_e} = \frac{1}{\sqrt{2}}\sqrt{(\sigma_{1_e} - \sigma_{2_e})^2 + (\sigma_{2_e} - \sigma_{3_e})^2 + (\sigma_{3_e} - \sigma_{1_e})^2 + 6(\sigma_{4_e}^2 + \sigma_{5_e}^2 + \sigma_{6_e}^2)} \tag{4.9}$$

The von Mises stress as determined by equation 4.9 cannot have a negative value, and thus the positive effect of compressive mean stresses is not considered. Therefore, in order to take these effects into account the sign of the mean stress is to be determined. The sign of the mean stresses can be determined by different approaches, either by the sign of the maximum absolute principal stress or by the sign of the hydrostatic mean stress. Here the sign is determined from the hydrostatic stresses after correspondence with Grundfos. The sign is found for each element and load cycle.

$$sign_{e_i} = sign(c_{m_i}(\sigma_{1_e} + \sigma_{2_e} + \sigma_{3_e})) \tag{4.10}$$

$$\sigma_{vm,a_{e_i}} = c_{a_i}\sigma_{vm_e} \tag{4.11}$$

$$\sigma_{vm,m_{e_i}} = sign_{e_i}\sqrt{c_{m_i}^2}\sigma_{vm_e} \tag{4.12}$$

Note that the sign function is non differentiable, however this appears to cause no issues of convergence, based on observations from numerical experiments. The equivalent uniaxial amplitude stress necessary for using the S-N curves is obtained by taking into account the compressive mean stresses. From experimental data, it has been determined that tensile mean stresses have a negative effect on fatigue life, while compressive mean stresses have a positive effect for a given amplitude stress. There exist a number of equations that attempts to capture this phenomena, such as the Gerber parabola, the Modified Goodman equation and the Morrow line (Stephens et al., 2001). The Gerber parabola fails to take into account the positive aspects of compressive mean stresses, and is therefore not considered. Both the modified Goodman equation and the Morrow line take these positive effects into account, here the modified Goodman equation is used.

$$\tilde{\sigma}_{svm\,e_i} = \left(\frac{\sigma_u}{\sigma_u - \sigma_{vm,m_{e_i}}}\right)\sigma_{vm,a_{e_i}} \tag{4.13}$$

Here σ_u is the ultimate tensile strength of the considered material. Considering the term which determines the mean stress effects that is multiplied with the equivalent amplitude. In this term it can be seen that there is a vertical asymptote at $\sigma_{vm,m_{e_i}} = \sigma_u$, if $\sigma_{vm,m_{e_i}} > \sigma_u$ the mean stress effects would become negative, resulting in a negative uniaxial equivalent amplitude stress, since $\sigma_{vm,a_{e_i}} \geq 0$. This issue might cause some convergence issues if large positive mean stresses occur, but this problem can be mitigated by using combined fatigue and yield constraints which would ensure that the mean stresses are below the ultimate tensile strength. Figure 4.5 illustrates the feasible region as determined by the modified Goodman equation and the yield limits.

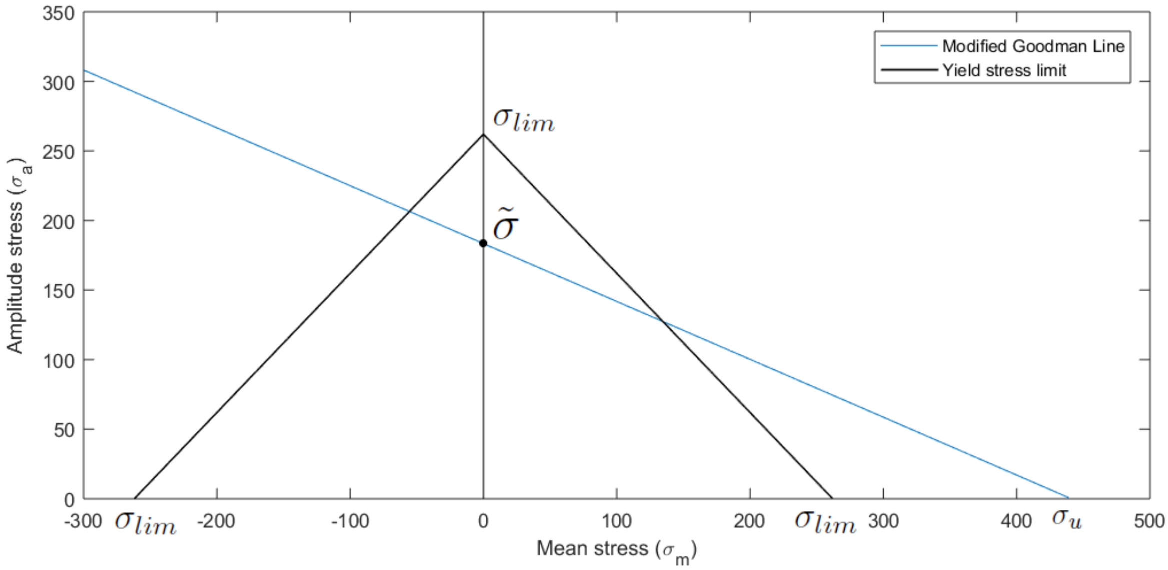

Figure 4.5: Feasible region as determined by modified Goodman equation and yield limits

Here the yield stress limits are indicated by the black lines, and the modified goodman line by the blue. For a given combination of amplitude σ_a and mean σ_m stress, gives an equivalent stress $\tilde{\sigma}$ where line Goodman line intersects the zero mean stress line.

4.3 S-N Curve

S-N curves are experimentally generated stress-life curves for a given material in a uni-axial stress state. The S-N curve estimates the number of cycles to failure N_f as defined in the experimental test, from the applied stress range or stress amplitude. Generally the S-N curve consists of 2 possibly 3 stages dependent on the material, a low cycle region from $1 - 10^3$ cycles, this region is characterised by plastic deformation and lends itself best to strain-life models. High cycle fatigue is generally defined from cycles above 10^3, here the strains are considered elastic, and this is the region which is the concern of this thesis, since the structures are also constrained by the yield stress. Some materials contain a third region known as the endurance region, from cycles above approximately 10^6 or 10^7. Here the estimated number of cycles to failure creates no damage.

The S-N curve is here approximated using the Basquin curve as proposed in Stephens et al. (2001) which represents a straight line in a log-log plot as illustrated in figure 4.6.

$$\tilde{\sigma}_{e_i} = \sigma'_f (2N_{f,e_i})^b \tag{4.14}$$

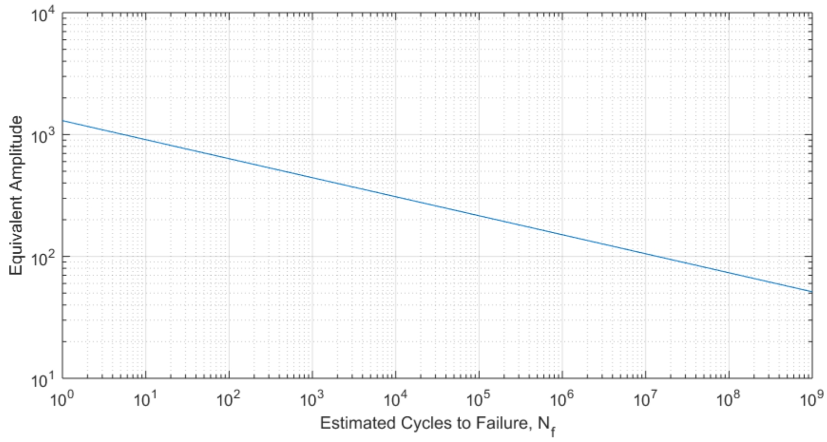

Figure 4.6: Basquin Curve

From (4.14) it is possible to estimate the number of cycles failure at each element for each rainflow N_{f,e_i}. This is done based on the equivalent uni-axial amplitude stress, and the material parameters σ_f' which is the fatigue strength coefficient and b which represents the slope of the S-N curve in the log-log plot shown in figure 4.6.

More complicated S-N curves can be implemented, however as noted in Oest and Lund (2017b) if S-N curves with an endurance limit is considered, there might occur some issues with removing material in low damage region, since the sensitivity of the damage with respect to the equivalent uniaxial amplitude stress is zero, if they are below this endurance limit. This might be mitigated by imposing a small slope to the S-N curve after the endurance limit.

4.4 Damage Accumulation

Since the structure is subjected to variable loading, the notion of damage is introduced. Damage is defined as the fraction of life that is used by an event in the load history. In Palmgren-Miners linear damage rule the damage caused by a single reversal is defined as the following.

$$D = \frac{1}{N_f} \tag{4.15}$$

Here D is the damage and N_f is the estimated number of cycles to failure for that reversal. According to the linear damage hypothesis the failure of a structure is predicted, when the accumulated damage of all reversals reaches a critical value μ. The notion of damage is here extended to an element basis, such that for each element not to fail it must uphold the following condition, where the damage is accumulated over the number of rainflows n_{RF}.

$$D_e = c_d \sum_{i=1}^{n_{RF}} \frac{1}{N_{f,e_i}} \leq \mu \tag{4.16}$$

Since the rainflow counting is performed on a representative section of the complete load history, determined by k number of loads, the load history scaling factor c_d is introduced to scale the damage from the representative section to the complete load history.

There are objections to the assumptions taken in Palmgren-Miners linear damage hypothesis. Such as that it neglects the interaction and sequence effects of the load history, and while there exits more complicated damage methods, Palmgren-Miners damage rule is still widely used since the more complicated methods yield no better prediction based on experimental data (Stephens et al., 2001)

4.5 Problem Formulation - Fatigue Constraint

Like the stress constraints, the element damage constraint is a local state. Therefore, for computational reasons the P-norm aggregate function is used.

$$\Psi = \left(\sum_{e=1}^{n_e} D_e^P \right)^{\frac{1}{P}} \tag{4.17}$$

For the reasons outlined in section 3.4 the adaptive constraint scaling factor is likewise used in combination with the aggregated damage constraint. The optimization problem considering minimum mass while being subjected to a fatigue constraints, can now be established as the following.

$$\begin{aligned} \underset{\rho}{\text{minimize}} \quad & f = \frac{1}{V_0} \sum_{e=1}^{n_e} v_e \tilde{\rho}_e \\ \text{subject to} \quad & g = \left(\frac{c^{(I)} \Psi}{\mu} \right) \leq 1 \\ & \rho_e = [\rho_{min}, 1] \end{aligned} \tag{4.18}$$

Sensitivity Analysis 5

In order to efficiently solve the optimization problem gradient based optimization methods are utilized. Specifically first order gradient based methods, and thus the gradient of the objective function and the constraint with respect to the design variables are required. The gradients are here analytically determined using the adjoint formulation, since the number of constraints are fewer than the number of design variables due to use of the aggregate function (Christensen and Klabring, 2009). The gradients are here presented using numerator-layout notation.

All the objectives and constraints are evaluated based on the physical density variables, which are determined by the filtering techniques on the design variables. Therefore, the chain rule must first be applied to determine the sensitivity of the physical variables. Here f serves as both the objective and constraint function.

$$\frac{df}{d\rho_j} = \frac{df}{d\tilde{\rho}_e}\frac{d\tilde{\rho}_e}{d\rho_j} \tag{5.1}$$

The gradient $\frac{d\tilde{\rho}_e}{d\rho_j}$ is determined by differentiating the density filter given by (2.8).

$$\frac{d\tilde{\rho}_e}{d\rho_j} = \frac{\omega_j}{\sum\limits_{j=1}^{n_e}\omega_j} \tag{5.2}$$

If the threshold filter is applied see (2.10), an extra term in chain rule expansion is necessary, such that the sensitivity with respect to the design variables is the following.

$$\frac{df}{d\rho_j} = \frac{df}{d\tilde{\rho}_e}\frac{d\tilde{\rho}_e}{d\tilde{\rho}_e^*}\frac{d\tilde{\rho}_e^*}{d\rho_j} \tag{5.3}$$

The final term in the above expression is the same as established in (5.2). The middle term is obtained by differentiating (2.10) with respect to the filtered density variable.

$$\frac{d\tilde{\rho}_e}{d\tilde{\rho}_e^*} = -\frac{\beta\left(tanh\left(\beta\left(\eta - \tilde{\rho}_e^*\right)\right)^2 - 1\right)}{tanh\left(\beta\eta\right) - tanh\left(\beta\left(\eta - 1\right)\right)} \tag{5.4}$$

In this chapter only the stress and fatigue optimization problems are considered, for a derivation of the sensitivities related to the minimum compliance optimization refer to Bendsøe and Sigmund (2003).

5.1 The Objective Function

The objective function for both optimization problem formulations (3.16) and (4.18) is to minimize the mass. As stated previously the mass is determined based on the physical variables, and thus the sensitivity can be found to be the element volume normalized with the domain volume.

$$\frac{df}{d\tilde{\rho}_e} = \frac{v_e}{V_0} \tag{5.5}$$

5.2 The Constraint Functions

The following sections will establish the sensitivity with respect to the physical density variables of the three constraint functions namely, the von Mises constraint and the two fatigue constraints based on either the Sines criterion or the signed von Mises. Initially the adjoint formulation is established, then a chain rule expansion of the three constraints is performed, and lastly the terms in the chain rule expansions are determined.

5.2.1 Adjoint Formulation

The constraint functions are all explicitly dependent on the physical design variables and implicitly dependent on them through the displacements, as determined by the equilibrium equations. Thus in order to obtain the first order derivative of the constraint equations the total derivative is taken.

$$\frac{dg}{d\tilde{\rho}_e} = \frac{\partial g}{\partial \tilde{\rho}_e} + \frac{\partial g}{\partial \boldsymbol{D}} \frac{d\boldsymbol{D}}{d\tilde{\rho}_e} \tag{5.6}$$

Here, the first term on the right-hand side captures the explicit dependence on the design variables, while the second term is the implicit dependence through the displacements. The last part of the second term on the right-hand side $\frac{d\boldsymbol{D}}{d\tilde{\rho}_e}$ can now be expressed by differentiating the equilibrium equations (2.3).

$$\frac{d\boldsymbol{K}}{d\tilde{\rho}_e}\boldsymbol{D} + \boldsymbol{K}\frac{d\boldsymbol{D}}{d\tilde{\rho}_e} = \frac{d\boldsymbol{R}}{d\tilde{\rho}_e} \tag{5.7}$$

In this case the forces are assumed independent from the design variables, thus its derivative is zero.

$$\frac{d\boldsymbol{K}}{d\tilde{\rho}_e}\boldsymbol{D} + \boldsymbol{K}\frac{d\boldsymbol{D}}{d\tilde{\rho}_e} = \boldsymbol{0} \tag{5.8}$$

Isolating the sensitivity of the displacements.

$$\frac{d\boldsymbol{D}}{d\tilde{\rho}_e} = -\boldsymbol{K}^{-1}\frac{d\boldsymbol{K}}{d\tilde{\rho}_e}\boldsymbol{D} \tag{5.9}$$

This expression is then substituted back into (5.6).

$$\frac{dg}{d\tilde{\rho}_e} = \frac{\partial g}{\partial \tilde{\rho}_e} - \frac{\partial g}{\partial \boldsymbol{D}}\boldsymbol{K}^{-1}\frac{d\boldsymbol{K}}{d\tilde{\rho}_e}\boldsymbol{D} \tag{5.10}$$

Now the global adjoint problem is formulated, where the global adjoint vector $\boldsymbol{\lambda}$ is found by solving the following equations.

$$\boldsymbol{K}\boldsymbol{\lambda} = \left(\frac{\partial g}{\partial \boldsymbol{D}}\right)^T \tag{5.11}$$

The adjoint vector is then substituted in (5.10).

$$\frac{dg}{d\tilde{\rho}_e} = \frac{\partial g}{\partial \tilde{\rho}_e} - \boldsymbol{\lambda}^T\frac{d\boldsymbol{K}}{d\tilde{\rho}_e}\boldsymbol{D} \tag{5.12}$$

The gradient on an element level is formulated by extracting the degrees of freedom associated with element e from the global displacement vector $\boldsymbol{D}$ and the global adjoint vector $\boldsymbol{\lambda}$, denoted as $\boldsymbol{d}_e$ and $\boldsymbol{\lambda}_e$. Furthermore, since the global stiffness matrix $\boldsymbol{K}$ is assembled from the element stiffness matrices $\boldsymbol{K}_e$, only the element stiffness matrix associated with element e is differentiated.

$$\frac{dg}{d\tilde{\rho}_e} = \frac{\partial g}{\partial \tilde{\rho}_e} - \boldsymbol{\lambda}_{\boldsymbol{e}}^T \frac{d\boldsymbol{K}_e}{d\tilde{\rho}_e} \boldsymbol{d}_e \tag{5.13}$$

Now, the first term on the right-hand side of (5.13) $\frac{\partial g}{\partial \tilde{\rho}_e}$, and the element wise contribution to the sensitivity term in the adjoint vector $\frac{\partial g}{\partial \boldsymbol{d}_e}$ is found for each of the constraints. In the following section each of the three constraint are expanded using the chain rule. Subsequently, each of the expanded terms are obtained, since many of the expanded terms are identical in the three constraints.

5.2.2 Chain Rule Expansion

This section establishes the individual sensitivity terms by chain rule expansion of the constraint functions differentiated with respectively the physical density variable and the element displacements.

Von Mises Constraint

The gradient of the von Mises stress constraint is found by applying the chain rule to the constraint in (3.16), resulting in the following.

$$\frac{\partial g}{\partial \tilde{\rho}_e} = \frac{\partial \Psi}{\partial \sigma_{vm\,e}} \frac{\partial \sigma_{vm\,e}}{\partial \boldsymbol{\sigma}_e} \frac{\partial \boldsymbol{\sigma}_e}{\partial \tilde{\rho}_e} \tag{5.14}$$

$$\frac{\partial g}{\partial \boldsymbol{d}_e} = \frac{\partial \Psi}{\partial \sigma_{vm\,e}} \frac{\partial \sigma_{vm\,e}}{\partial \boldsymbol{\sigma}_e} \frac{\partial \boldsymbol{\sigma}_e}{\partial \boldsymbol{d}_e} \tag{5.15}$$

Where the first term $\frac{\partial \Psi}{\partial \sigma_{vm\,e}}$ is the aggregate function (3.11) differentiated with respect to the element von Mises stress. Afterwards the von Mises stress is differentiated with respect to the element stress components $\frac{\partial \sigma_{vm\,e}}{\partial \boldsymbol{\sigma}_e}$. The final terms in (5.14) and (5.15) are the element stress components differentiated with the physical density variable and the element displacement respectively.

Sines Constraint

We now consider the fatigue constraint based on the Sines criterion. The chain rule expansion yields the following equations.

$$\frac{\partial g}{\partial \tilde{\rho}_e} = \frac{\partial \Psi}{\partial D_e} \sum_{i=1}^{n_{RF}} \frac{\partial D_e}{\partial N_{f,e_i}} \frac{\partial N_{f,e_i}}{\partial \tilde{\sigma}_{sines\,e,i}} \left(c_{a_i} \frac{\partial \tilde{\sigma}_{sines\,a_e}}{\partial \boldsymbol{\sigma}_e} + c_{m_i} \frac{\partial \tilde{\sigma}_{sines\,m_e}}{\partial \boldsymbol{\sigma}_e} \right) \frac{\partial \boldsymbol{\sigma}_e}{\partial \tilde{\rho}_e} \tag{5.16}$$

$$\frac{\partial g}{\partial \boldsymbol{d}_e} = \frac{\partial \Psi}{\partial D_e} \sum_{i=1}^{n_{RF}} \frac{\partial D_e}{\partial N_{f,e_i}} \frac{\partial N_{f,e_i}}{\partial \tilde{\sigma}_{sines\,e,i}} \left(c_{a_i} \frac{\partial \tilde{\sigma}_{sines\,a_e}}{\partial \boldsymbol{\sigma}_e} + c_{m_i} \frac{\partial \tilde{\sigma}_{sines\,m_e}}{\partial \boldsymbol{\sigma}_e} \right) \frac{\partial \boldsymbol{\sigma}_e}{\partial \boldsymbol{d}_e} \tag{5.17}$$

The first term $\frac{\partial \Psi}{\partial D_e}$ is the partial derivative of the aggregate function with the element damage established in (4.17). The subsequent terms has to summed over the number of rainflows, due to the cumulative nature of Palmgren-Miners damage rule (4.16). The first term within the sum

$\frac{\partial D_e}{\partial N_{e,i}}$ is the partial derivative of the damage with respect to the estimated number of cycles to failure at element e for the $i'th$ rainflow, then the estimated number of cycles to failure (4.14) is differentiated with the Sines equivalent stress (4.8). Since the Sines equivalent stress is a sum of an equivalent amplitude (4.6) and an equivalent mean stress (4.7), the derivative of the equivalent stress is separated using the summation rule. The derivative of the equivalent amplitude and mean stress are calculated with respect to the reference stress at element e and then scaled with the amplitude and mean constants for the $i'th$ rainflow. Lastly, the final term is the derivative of the element stress with respect to either the physical variables or the reference displacement.

Signed von Mises Constraint

The sensitivity of the signed von Mises fatigue criterion (4.13) is found similarly to constraint based on the Sines criterion, however with the introduction of the sign function and the mean stress effects based on the equivalent mean and amplitude von Mises stress.

$$\frac{\partial g}{\partial \tilde{\rho}_e} = \frac{\partial \Psi}{\partial D_e} \sum_{i=1}^{n_{RF}} \frac{\partial D_e}{\partial N_{f,e_i}} \frac{\partial N_{f,e_i}}{\partial \tilde{\sigma}_{svm\,e,i}} \left(c_{a_i} \frac{\partial \tilde{\sigma}_{svm\,e}}{\partial \sigma_{vm\,a_e}} \frac{\partial \tilde{\sigma}_{vm\,a_e}}{\partial \boldsymbol{\sigma}_e} + sign_{e_i} \sqrt{c_{m_i}^2} \frac{\partial \tilde{\sigma}_{svm\,e}}{\partial \sigma_{vm\,m_e}} \frac{\partial \tilde{\sigma}_{vm\,m_e}}{\partial \boldsymbol{\sigma}_e} \right) \frac{\partial \boldsymbol{\sigma}_e}{\partial \tilde{\rho}_e} \tag{5.18}$$

$$\frac{\partial g}{\partial \boldsymbol{d}_e} = \frac{\partial \Psi}{\partial D_e} \sum_{i=1}^{n_{RF}} \frac{\partial D_e}{\partial N_{f,e_i}} \frac{\partial N_{f,e_i}}{\partial \tilde{\sigma}_{svm\,e,i}} \left(c_{a_i} \frac{\partial \tilde{\sigma}_{svm\,e}}{\partial \sigma_{vm\,a_e}} \frac{\partial \tilde{\sigma}_{vm\,a_e}}{\partial \boldsymbol{\sigma}_e} + sign_{e_i} \sqrt{c_{m_i}^2} \frac{\partial \tilde{\sigma}_{svm\,e}}{\partial \sigma_{vm\,e}} \frac{\partial \tilde{\sigma}_{vm\,e}}{\partial \boldsymbol{\sigma}_e} \right) \frac{\partial \boldsymbol{\sigma}_e}{\partial \boldsymbol{d}_e} \tag{5.19}$$

Now that the constraint sensitivity has been expanded using the chain rule, the individual components of the expanded terms can be found.

5.2.3 Sensitivity Terms

In the following section the individual terms present in the constraint functions chain rule expansion are found.

Aggregate functions

The first terms are (5.14) and (5.15) is the aggregate function differentiated with respect to the element von Mises stress.

$$\frac{\partial \Psi}{\partial \sigma_{vm\,e}} = \left(\sum_{i=1}^{n_e} \sigma_{vm\,i}^P \right)^{\frac{1}{P}-1} \sigma_{vm\,e}^{P-1} \tag{5.20}$$

Likewise, for both the Sines (5.16)(5.17) and signed von Mises (5.18)(5.19) the first term is the aggregate function differentiated with respect element damage.

$$\frac{\partial \Psi}{\partial D_e} = \left(\sum_{i=1}^{n_e} D_i^P \right)^{\frac{1}{P}-1} D_e^{P-1} \tag{5.21}$$

Damage

The partial derivative of the element damage as defined in 4.16 with respect to the estimated number of cycles to failure is given as.

$$\frac{\partial D_e}{\partial N_{f,e_i}} = -c_d \frac{1}{N_{e,i}^2} \tag{5.22}$$

Cycles To Failure

Here is the estimated number of cycles to failure differentiated with respect to the equivalent stress amplitude $\tilde{\sigma}_{e_i}$ which can be either the Sines method or the signed von Mises criterion.

$$\frac{\partial N_{f,e_i}}{\partial \tilde{\sigma}_{e,i}} = \frac{1}{2\sigma'_f b}\left(\frac{\tilde{\sigma}_{e,i}}{\sigma'_f}\right)^{\frac{1}{b}-1} \tag{5.23}$$

Mean Stress Effects

The mean stress effects found using the modified Goodman equation see (4.13) used in the signed von Mises criterion, is here differentiated with respect to the equivalent amplitude and mean von Mises stress.

$$\frac{\partial \tilde{\sigma}_{svm\,e}}{\partial \sigma_{vm\,a_e}} = \left(\frac{\sigma_u}{\sigma_u - \sigma_{vm,m_e}}\right) \tag{5.24}$$

$$\frac{\partial \tilde{\sigma}_{svm\,e}}{\partial \sigma_{vm\,m_e}} = \left(\frac{\sigma_u}{(\sigma_u - \sigma_{vm,m_e})^2}\right)\sigma_{vm,a_e} \tag{5.25}$$

Sines Equivalent Mean

Now, the sensitivity of the equivalent mean stress as defined in the Sines criterion (4.7) with respect to stress components is found.

$$\frac{\partial \tilde{\sigma}_{sines\,m_e}}{\partial \sigma_{1\,e}} = \frac{\partial \tilde{\sigma}_{sines\,m_e}}{\partial \sigma_{2\,e}} = \frac{\partial \tilde{\sigma}_{sines\,m_e}}{\partial \sigma_{3\,e}} = \frac{1}{\sqrt{2}}\beta \tag{5.26}$$

Von Mises stress - Sines Equivalent Amplitude

The sensitivity of the von Mises stress and the Sines equivalent amplitude stress with respect to the stress components in 3D is given as.

$$\frac{\partial \sigma_{vm\,e}}{\partial \sigma_{1\,e}} = \frac{\partial \tilde{\sigma}_{sines\,a_e}}{\partial \sigma_{1\,e}} = \frac{1}{2\sigma_{vm\,e}}\left(2\sigma_{1\,e} - \sigma_{2\,e} - \sigma_{3\,e}\right) \tag{5.27}$$

$$\frac{\partial \sigma_{vm\,e}}{\partial \sigma_{2\,e}} = \frac{\partial \tilde{\sigma}_{sines\,a_e}}{\partial \sigma_{2\,e}} = \frac{1}{2\sigma_{vm\,e}}\left(2\sigma_{2\,e} - \sigma_{1\,e} - \sigma_{3\,e}\right) \tag{5.28}$$

$$\frac{\partial \sigma_{vm\,e}}{\partial \sigma_{3\,e}} = \frac{\partial \tilde{\sigma}_{sines\,a_e}}{\partial \sigma_{3\,e}} = \frac{1}{2\sigma_{vm\,e}}\left(2\sigma_{3\,e} - \sigma_{1\,e} - \sigma_{2\,e}\right) \tag{5.29}$$

$$\frac{\partial \sigma_{vm\,e}}{\partial \sigma_{4\,e}} = \frac{\partial \tilde{\sigma}_{sines\,a_e}}{\partial \sigma_{4\,e}} = \frac{3}{\sigma_{vm\,e}}\sigma_{4\,e} \tag{5.30}$$

$$\frac{\partial \sigma_{vm\,e}}{\partial \sigma_{5\,e}} = \frac{\partial \tilde{\sigma}_{sines\,a_e}}{\partial \sigma_{5\,e}} = \frac{3}{\sigma_{vm\,e}}\sigma_{5\,e} \tag{5.31}$$

$$\frac{\partial \sigma_{vm\,e}}{\partial \sigma_{6\,e}} = \frac{\partial \tilde{\sigma}_{sines\,a_e}}{\partial \sigma_{6\,e}} = \frac{3}{\sigma_{vm\,e}}\sigma_{6\,e} \tag{5.32}$$

Stress components

In each constraint sensitivity equation, the sensitivity of the element stress vector is needed, first with respect to the physical density and second with respect to the element displacement, this is obtained by differentiating (3.10).

$$\frac{\partial \boldsymbol{\sigma}_e}{\partial \tilde{\rho}_e} = qp\, \tilde{\rho}_e^{(qp-1)} \boldsymbol{C}(E_0)\boldsymbol{B}\boldsymbol{d}_e \tag{5.33}$$

$$\frac{\partial \boldsymbol{\sigma}_e}{\partial \boldsymbol{d}_e} = \tilde{\rho}_e^{qp} \boldsymbol{C}(E_0)\boldsymbol{B} \tag{5.34}$$

Stiffness matrix

The final part of the sensitivity analysis is to obtain the sensitivity of the element stiffness matrix with respect to the physical variables (5.13). This is accomplished by differentiating the element stiffness matrix see (2.4) which is composed of the effective modulus of elasticity defined by the modified SIMP definition (2.2) and the element stiffness matrix evaluated for a unit modulus of elasticity $\boldsymbol{K}_0$.

$$\frac{d\boldsymbol{K}_e}{d\tilde{\rho}_e} = \boldsymbol{K}_0 \left(p\left(E_0 - E_{min}\right) \tilde{\rho}_e^{(p-1)} \right) \tag{5.35}$$

Numerical Examples 6

This chapter presents the numerical experiments which illustrate the previously established topology optimization problem formulations, based on the von Mises yield constraint, as well as the two fatigue constraints, one based on the Sines criterion and the other on the signed von Mises criterion. Some of the general considerations regarding the use of fatigue constraints are illustrated on 2D examples, where the effects are easier to illustrate. The 2D examples are all assumed to be in plane stress.

All the optimization problems are performed using the material AISI 1020 HR steel with the material data obtained from Stephens et al. (2001). Regarding the damage constraint formulated using Palmgren-Miners linear damage hypothesis (4.16) the critical value is $\mu = 1$.

Material Data - AISI 1020 HR Steel	
E_0	203 GPa
ν	0.3
b	-0.156
σ_{lim}	262 MPa
σ_u	441 MPa
σ'_f	1384 MPa
μ	1

Table 6.1: Material Data for AISI 1020 HR Steel

The topology optimization formulations established in this thesis are implemented as extensions to the minimum compliance topology optimization codes made available by the TopOpt group at DTU. All 2D examples are based upon the 88 line MATLAB code described in Andreassen et al. (2011), and as mentioned previously, the 3D examples are based upon the code implemented in the PETSc framework described in Aage et al. (2015). These codes provide the minimum compliance formulation, the FEM analysis for solving the static analysis problem, the filtering techniques (except the threshold filter) and the optimization solvers. In order to generate the load history the default random number generator is used in both c++ and MATLAB.

The optimization problems are all solved using the Method of Moving Asymptotes (MMA) optimization algorithm, outlined in Svanberg (1987), Svanberg (2007) and with parallel implementation in the PETSc framework in Aage and Lazarov (2013). The general idea behind MMA is to solve approximated sub-problems of the original problem, where these approximated problems are convex such that they can be easily solved. The approximated functions are based on information of the function value and first order derivatives at the current iteration, and if available, information from previous iterations of the design variables, and the lower and upper asymptotes used to generate the approximate convex functions.

Based on recommendations in Svanberg (2007) the factors that determine the increase and decrease of the asymptotes, are decreased to 1.05 and 0.65, due to the high non-linearity of the optimization problems. Other parameters are left to the default values, if nothing else is indicated.

If nothing else is noted the optimization problems are solved with a P value of 12, and a continuation scheme is applied to the qp factor where it is reduced by 0.025 every 10^{th} iteration from 0.75 to 0.5. Furthermore, external move limits of 0.1 are applied.

6.1 Benchmark Problems

This section presents the benchmark examples used in the topology optimization. The benchmark examples are chosen based on the ability to compare results with other formulations present in the literature. Furthermore, the benchmark examples are chosen in order to illustrate some of the characteristics of using fatigue constraints. The 2D benchmark examples have unit thickness and the applied force is generally distributed over a number of elements, in order to avoid local stress singularities for both 2D and 3D.

6.1.1 2D Benchmark Examples

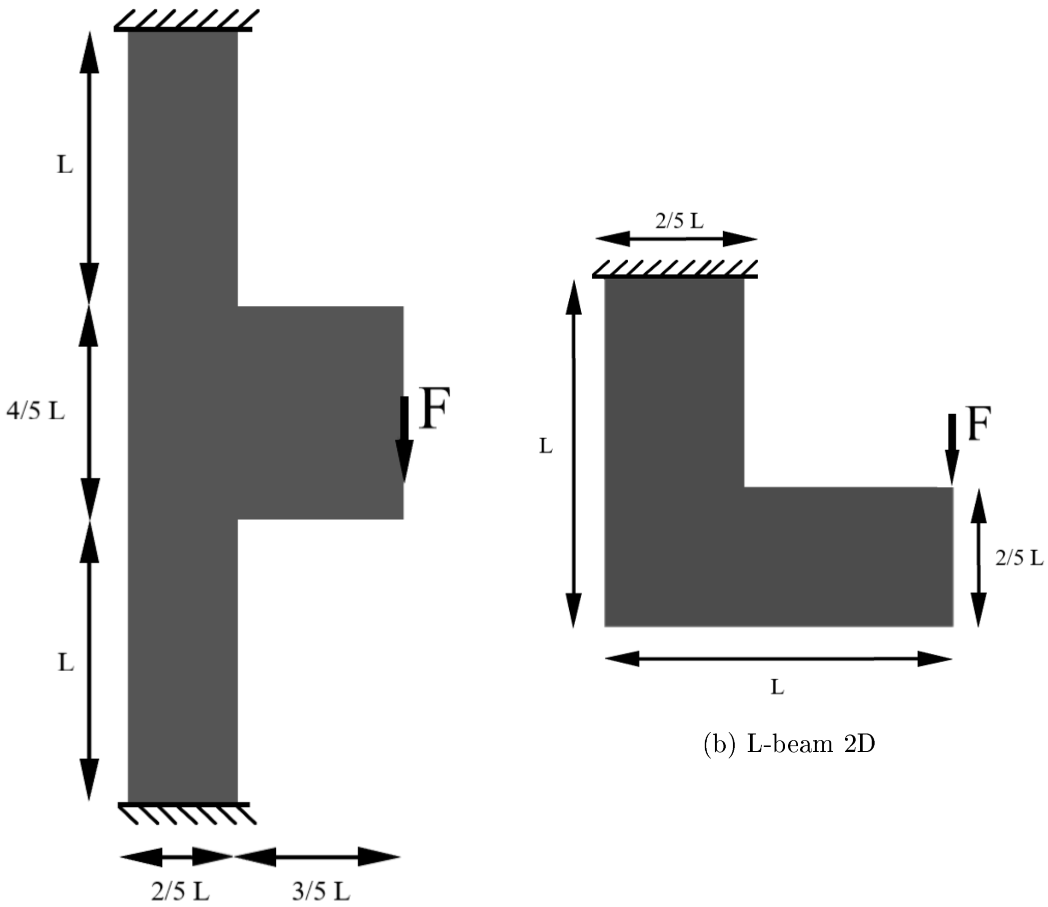

(a) Double L-beam 2D

(b) L-beam 2D

Figure 6.1: Benchmark examples for 2D

6.1.2 3D Benchmark Examples

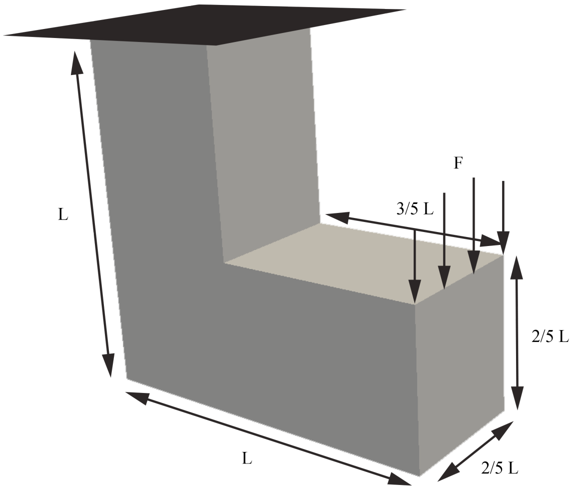

(a) L-beam 3D

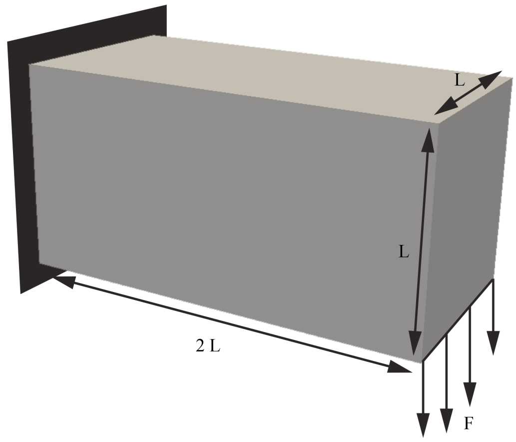

(b) Cantilever Beam 3D

Figure 6.2: Benchmark examples for 3D

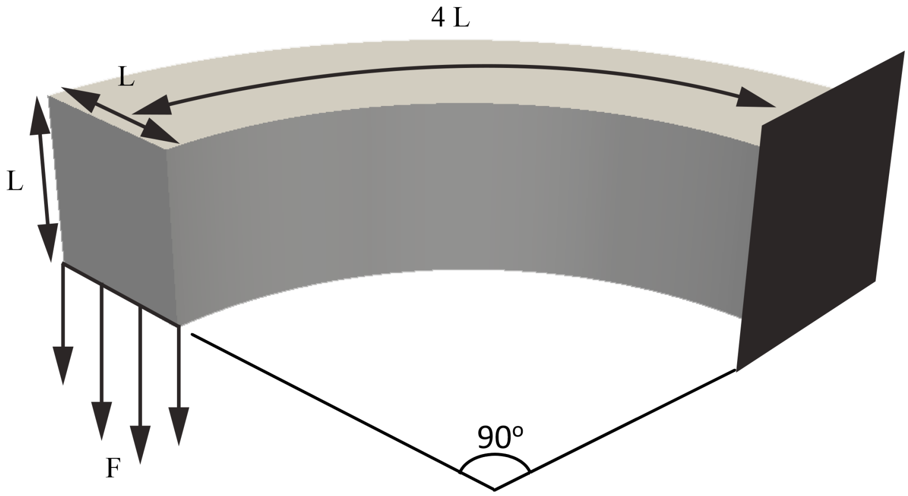

Figure 6.3: Curved Beam 3D

6.2 Benefits of Combined Fatigue & Yield Constraints

In Oest and Lund (2017b) where the fatigue constraints are included directly in the topology optimization formulation, the highly non-linear behaviour of the fatigue constraints compared with the von Mises constraint is highlighted. Similar results were experienced here when performing mass minimization with a fatigue constraint based on both Sines and signed von Mises equivalent stress. However the beneficial aspects on convergence of including a von Mises constraint in combination with a fatigue constraint were observed and will be illustrated on the following representative example, using a fatigue constraint based on Sines criterion.

The example will here be illustrated for the 2D double L-beam with L=120mm in figure 6.1a, a filter radius of 0.03L, and discretized using $n_e = 23040$ elements in order to facilitate comparison with the literature. All three examples are subjected to the same randomly generated load history with r = -1, corresponding to a fully reversed load, for k = 1000 loads using a reference force of 500N, the force is distributed across six elements. This is then scaled to full lifetime by $c_d = 1000$.

In all examples both the damage and von Mises stress distribution is shown, no matter the applied constraint, in order to show the effects one constraint has on the other.

6.2.1 Von Mises Yield Constraint

The following section illustrates the topology optimization considering minimum mass while being subjected to a single von Mises yield constraint. The optimization results are as follows.

Optimization Result	
f	0.1743
Iter	320
$max\left(\frac{D_e}{\mu}\right)$	32.6301
$max\left(\frac{\sigma_{vm}}{\sigma_{lim}}\right)$	1.0000

Table 6.2: Optimization results for minimum mass subjected to a von Mises yield constraint

As illustrated in figure 6.4 when performing the optimization solely with the von Mises constraint, the final result is a symmetric structure, with rounded corners to remove the stress concentrations that arise due to the re-entrant corners. The von Mises stress is equally distributed over the structure to fully utilize the material. When considering the damage in the structure, it is clearly visible that nearly all elements of the structure are greater than 1, with the maximum being above 32.

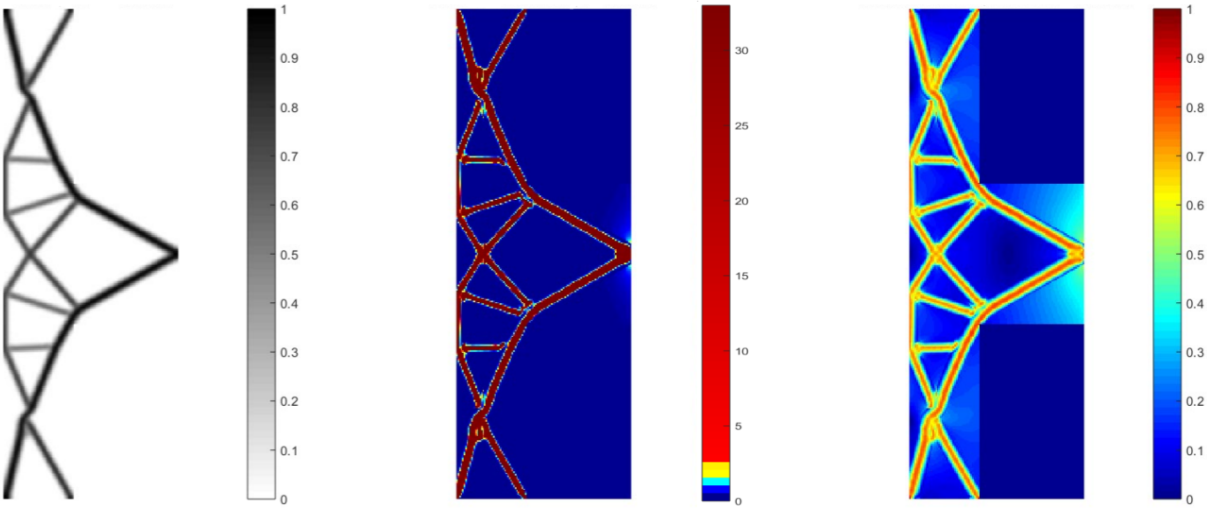

Figure 6.4: Yield constraint r = -1
The damage and von Mises stress are normalized with respect to μ and σ_{lim} respectively.
left: Density mid: Damage right: von Mises Stress

Considering the iteration history in figure 6.5, it is visible that the convergence of this optimization problem is quite smooth, with only minor jumps in both the objective function and constraint, and that the fatigue constraint is greater than 1 during the whole optimization procedure.

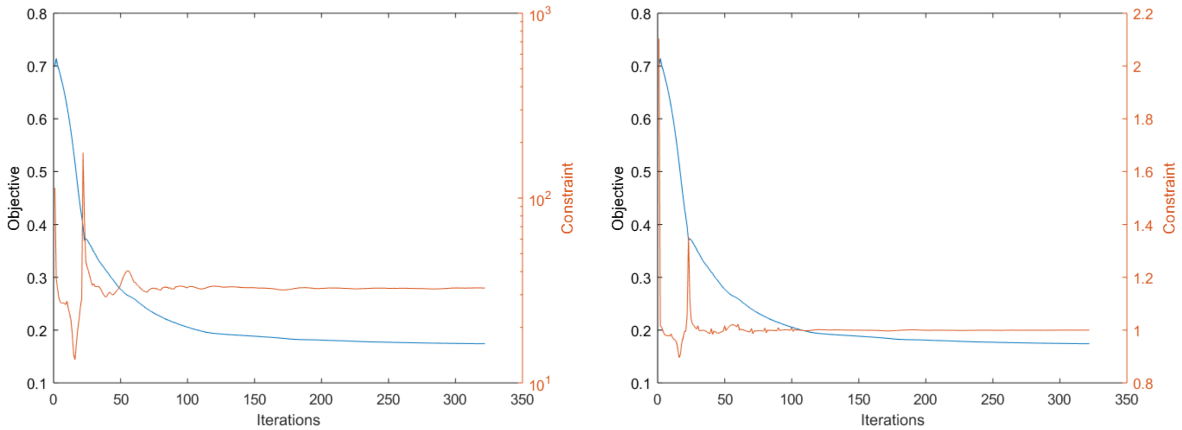

(a) Iteration history - Fatigue (Sines) constraint (b) Iteration history - Von Mises constraint

Figure 6.5: Iteration history for single von Mises constraint

6.2.2 Fatigue (Sines) Constraint

Using the same inputs, the problem is now solved considering the same objective while being subjected to a fatigue constraint based on Sines criterion. Comparing the optimization results in table 6.3 with 6.2 it can be seen that using the fatigue constraint results in a heavier structure.

Optimization Result	
f	0.2290
Iter	936
$max\left(\frac{D_e}{\mu}\right)$	0.9953
$max\left(\frac{\sigma_{vm}}{\sigma_{lim}}\right)$	0.5899

Table 6.3: Optimization results for minimum mass subjected to a fatigue (Sines) constraint

Contrasting the result obtained when considering the Sines fatigue constraint as illustrated in figure 6.6, with the results obtained using von Mises constraint in figure 6.4, it is clear that the final structure is substantially non symmetric. The final structure satisfies the damage constraint, with a satisfactory distribution, though there are some low damage regions.

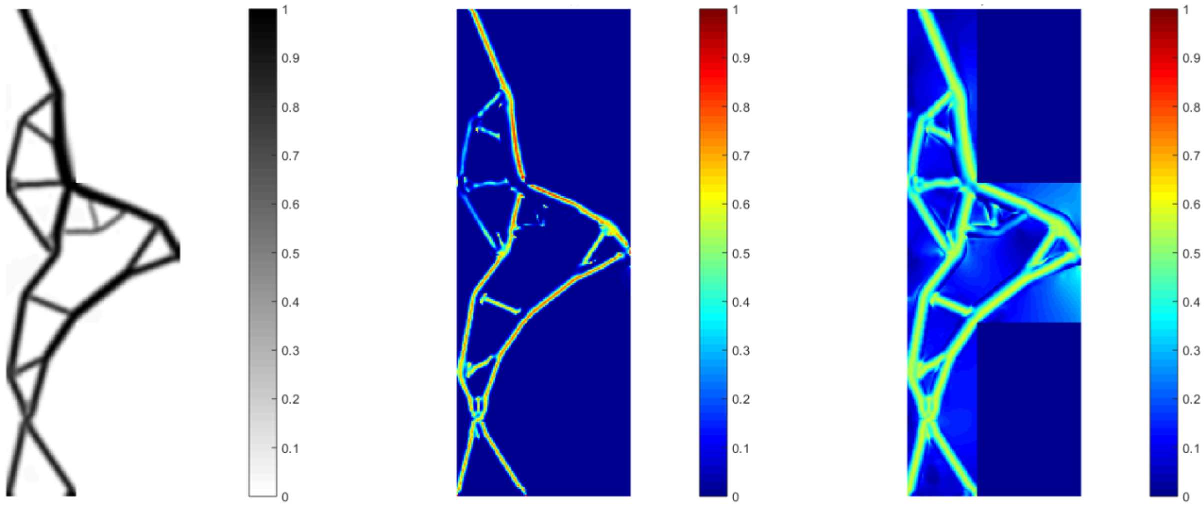

Figure 6.6: Fatigue (Sines) constraint r = -1
The damage and von Mises stress are normalized with respect to μ and σ_{lim} respectively.
left: Density mid: Damage right: von Mises Stress

Considering the von Mises stress distribution in figure 6.6 it can be seen that all the values are relatively low, with the majority having a normalized value of approximately 0.55.

Referring to the iteration history considering the fatigue constraint in figure 6.7a the non linear behaviour of the fatigue constraint is clear, there are multiple considerable jumps in both the objective function and the fatigue constraint, with maximum constraint violation during the optimization of 10^4.

Considering the number of iterations necessary for convergence, using the fatigue constraint requires nearly three times as many iterations as the von Mises constraint.

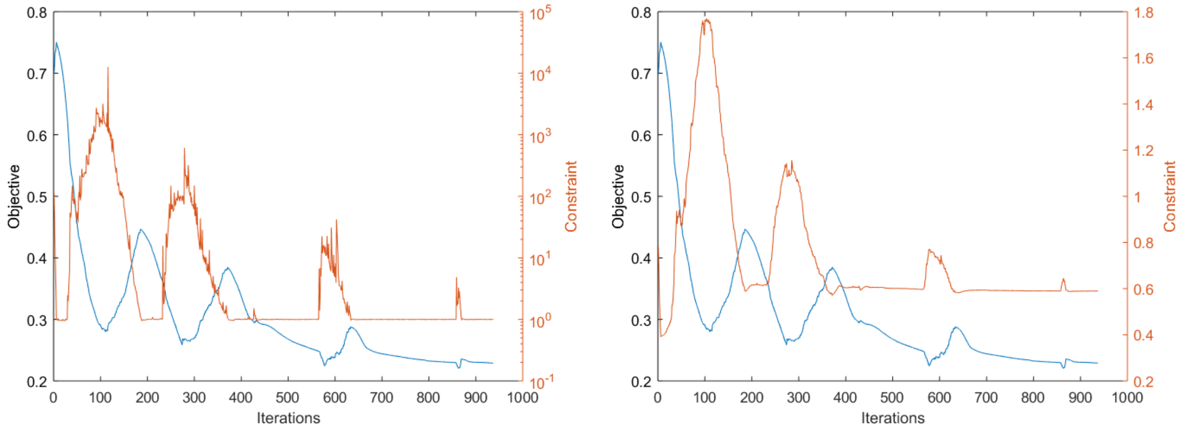

(a) Iteration history - Fatigue (Sines) constraint

(b) Iteration history - Von Mises constraint

Figure 6.7: Iteration history for single fatigue (Sines) constraint

6.2.3 Combined Fatigue & Yield Constraints

Now, the problem is solved for combined fatigue and yield constraints.

Optimization Result	
f	0.2119
Iter	700
$max\left(\frac{D_e}{\mu}\right)$	0.9931
$max\left(\frac{\sigma_{vm}}{\sigma_{lim}}\right)$	0.6010

Table 6.4: Optimization results for minimum mass subjected to both a fatigue (Sines) and yield constraint

The following example was performed using combined Sines fatigue constraint and a von Mises yield constraint. Even though the optimization was still dominated by the fatigue constraint, the final structure achieve some of the symmetric layout obtained when using solely the von Mises constraint as illustrated in 6.4. Considering the iteration history 6.9, there still exists the jumps which were present when using solely the fatigue constraint, however the degree of the constraint violation was reduced by two orders of magnitude when combined with the von Mises constraint. This effect is also visible when considering the objective function, where the jumps are approximately a third as compared with the objective function illustrated in figure 6.7.

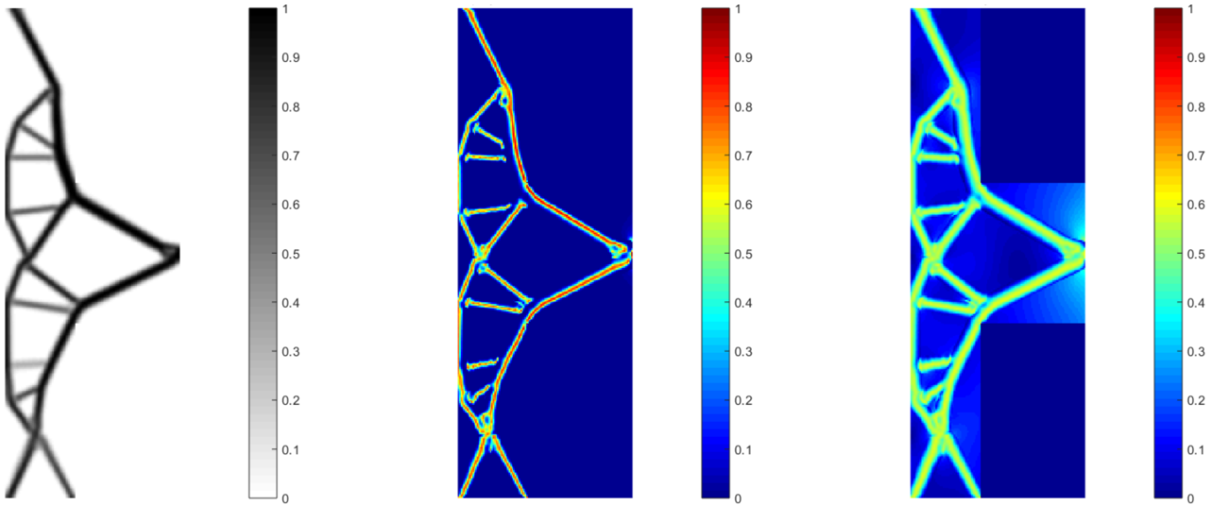

Figure 6.8: Yield & Fatigue (Sines) constraint r = -1
The damage and von Mises stress are normalized with respect to μ and σ_{lim} respectively.
left: Density mid: Damage right: von Mises Stress

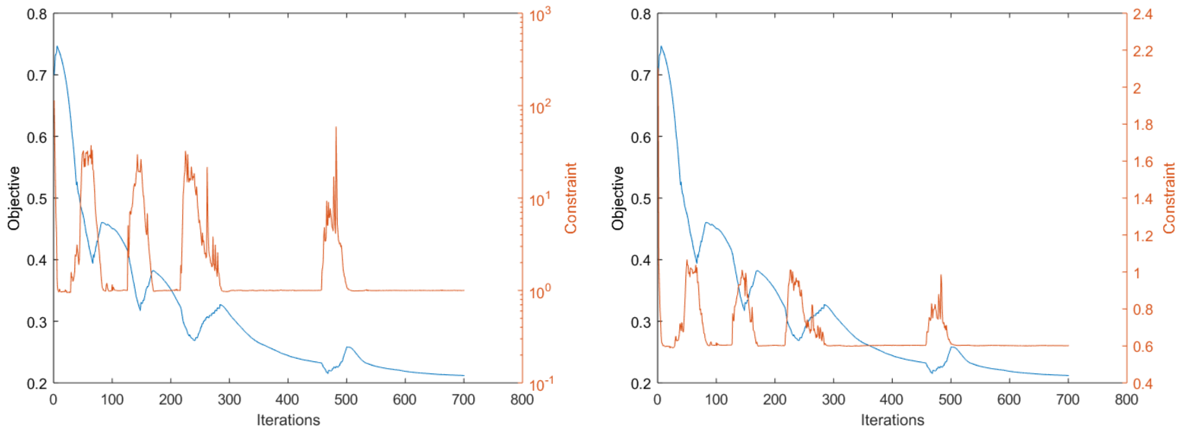

(a) Iteration history - Fatigue (Sines) constraint (b) Iteration history - Von Mises constraint

Figure 6.9: Iteration history for combined Fatigue (Sines) and von Mises constraint

6.2.4 Conclusion

The possible benefit of using combined fatigue and yield constraints have here been demonstrated on a representative example. When comparing the single fatigue constraint with the combined constraints, the combined constraints obtained a better objective function of $f = 0.2119$ as compared to $f = 0.2290$ for the fatigue constraint, in fewer iterations.

The beneficial aspect of using combined constraints are proportional to the degree of the yield constraints significance, such that the more dominant the yield constraint the better the convergence. In the example illustrated here, the normalized von Mises stress was generally around 0.6.

Using the combined constraints requires more computation compared to using a single fatigue constraint, since an additional adjoint problem has to be solved in order to obtain the von Mises constraint sensitivities. The large constraint violations present using the single fatigue constraint can be mitigated by imposing stricter move limits. However applying tighter move limits might further increase the already large number of iterations required for convergence.

In light of the previous points, the extra computational cost associated with combined constraints can be justified if the problem to be solved exhibits a highly non linear response exemplified by large constraint violations and poor convergence, which might lead to a sub optimal solution. Furthermore, the use of a single fatigue constraint does not guarantee sufficiently low stresses such that yielding does not occur, as illustrated in Oest and Lund (2017b) where two of the three examples presented had higher von Mises stresses than the yield stress limit, when solved for a fatigue constraint based on Sines criterion. A yield constraint is a general requirement for most structures, and is required not to violate the assumption of linear elasticity, which is required for the appropriate use of some of the aspects used in formulating the fatigue constraint.

6.3 Mean Stress Effects

In the following section the effects of mean stress is examined for the fatigue constraint based on the signed von Mises. The effects will be illustrated on the L-beam example shown in figure 6.1b with L=100mm in 6.1b, a filter radius of 0.03L and using $n_e = 6400$ elements, for the two most common r ratios, r=-1 which corresponds to a fully reversed loading and r=0 being pulsating positive loading between 0 and the reference load. The optimization problem is solved using a combined von Mises and fatigue constraint based on signed von Mises, due to the reasons laid forth in the previous section. Both examples are subjected to a reference load of $F_{ref} = 300$ and k = 1000. For r=-1 the load history is scaled with $c_d = 400$, and for r=0, $c_d = 20000$. The discrepancy in load history scaling is due to the fact that the load amplitude is different for two load ratios.

6.3.1 Load Ratio of r = -1

Optimization Result	
f	0.30584
Iter	705
$max\left(\frac{D_e}{\mu}\right)$	0.9950
$max\left(\frac{\sigma_{vm}}{\sigma_{lim}}\right)$	0.9982

For the first case, the load ratio is here set to r = -1, such that the load-history is fully reversed. As can be seen in figure 6.10 the damage and von Mises stress are equally distributed over the entire structure, which is to be expected, since the structure over the load history is approximately an equal amount in tension and compression.

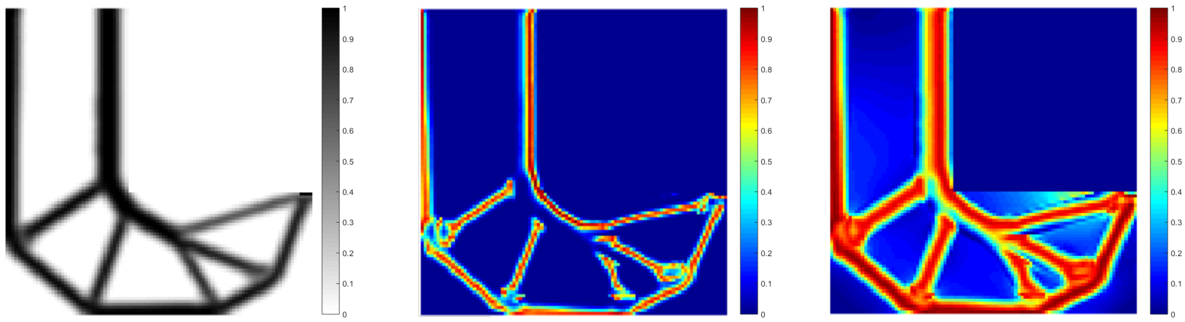

Figure 6.10: Yield & Fatigue (signed von Mises) constraint r = -1
The damage and von Mises stress are normalized with respect to μ and σ_{lim} respectively.
left: Density mid: Damage right: von Mises Stress

6.3.2 Load Ratio of r = 0

Optimization Result	
f	0.34192
Iter	755
$max\left(\frac{D_e}{\mu}\right)$	0.9965
$max\left(\frac{\sigma_{vm}}{\sigma_{lim}}\right)$	1.0002

Next, the optimization problem is solved for a load ratio of r = 0 which corresponds to a fluctuating positive load between 0 and the reference load. From figure 6.11 the positive effect of compressive stresses are evident when considering the damage distribution. Here it can be seen that the damage is far greater on the inside of the structure which is in tension, as compared to the outside of the structure that is in compression. Furthermore, when considering the von Mises stress distribution, it can be seen that the distribution is the opposite of the fatigue constraint. Here the outside of the structure has the highest stresses, while the inside is lower.

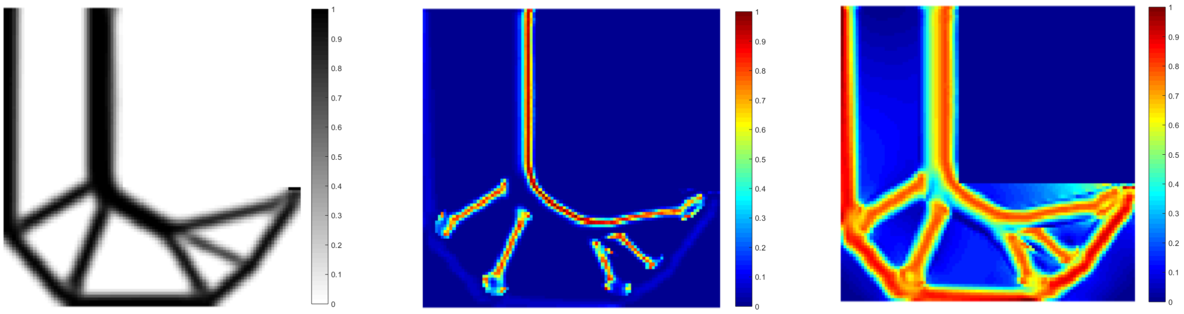

Figure 6.11: Yield & Fatigue (signed von Mises) constraint r = 0
The damage and von Mises stress are normalized with respect to μ and σ_{lim} respectively.
left: Density mid: Damage right: von Mises Stress

For this specific problem, the dominant failure mode is fatigue damage on the inside of the structure, and yielding on the outside. Thus especially for r = 0, the combination of both fatigue and yield constraints might be necessary, since yielding for the material considered is indiscriminate of tension and compression while fatigue is not. Therefore, if only a fatigue constraint is considered yielding might occur in the regions of compressive stress.

6.4 Large Scale Optimization in PETSc Framework

Even though 2D examples are useful, 3D structures are widely used, and thus, for topology optimization to be fully applicable in industrial settings should it be able to solve large 3D models. The following section will illustrate the applicability of the established topology optimization formulations for 3D problems.

The following examples are solutions to topology optimization problems formulated in the PETSc framework, utilizing parallel computing in order to address the problem of the additional computational resources necessary in order to solve large scale 3D problems. As mentioned previously the yield and fatigue constraints are implemented as an extension to the minimum compliance topology optimization problem provided by the TopOpt group at DTU and outlined in Aage et al. (2015). The framework is currently restricted to the use of structured grids, which makes parallelization easier, however this limits the geometrical complexity which can be solved using this framework. The domain used in structured grids is set along the Cartesian axis, producing a rectangular domain. This domain can then be modified by imposing void element sections, and by using mapping techniques, where the connectivity of the grid is maintained but the domain shape is transformed. The Rainflow counter and the ability to set void elements in the PETSc framework has been provided by Jacob Oest.

6.4.1 L beam

The following example is of the L beam illustrated in figure 6.2a which is solved in the PETSc framework, with a discretization of $n_e = 131072$ 1mm elements and filter radius of 2.4 element lengths. The L beam is subjected to a load of $F = 10000N$ with a fully reversed loading $r = -1$, k=1000 and a load history scaling factor of $c_d = 3000$. The L beam is first solved for minimum compliance, with an available volume constraint of $V^* = 0.35$ of the original domain. Afterwards a minimum mass objective is considered, first with a von Mises yield constraint, and then for a combined yield and fatigue constraint based on the signed von Mises criterion.

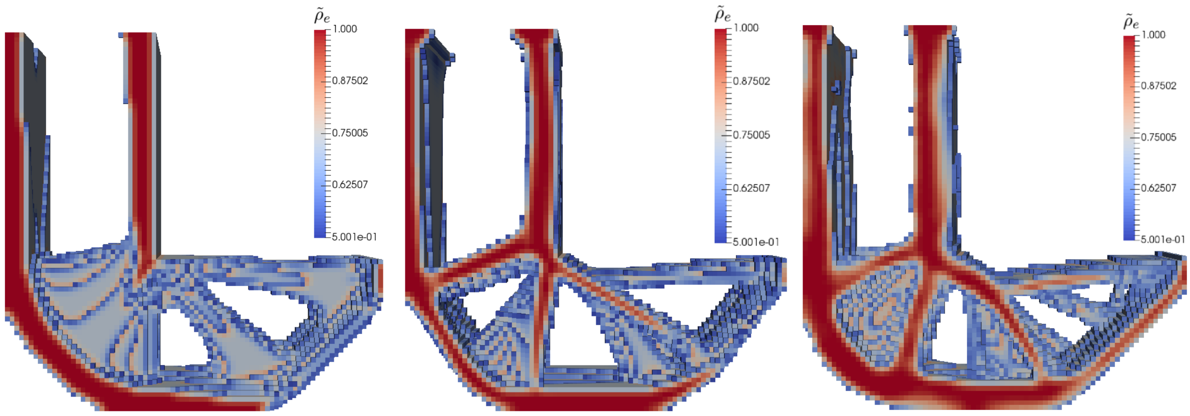

(a) Compliance minimization - Volume fraction

(b) Mass minimization - Von Mises

(c) Mass minimization - Fatigue (signed von Mises)

Figure 6.12: Density distribution illustrated with for $\tilde{\rho}_e \geq 0.5$ - Sideview

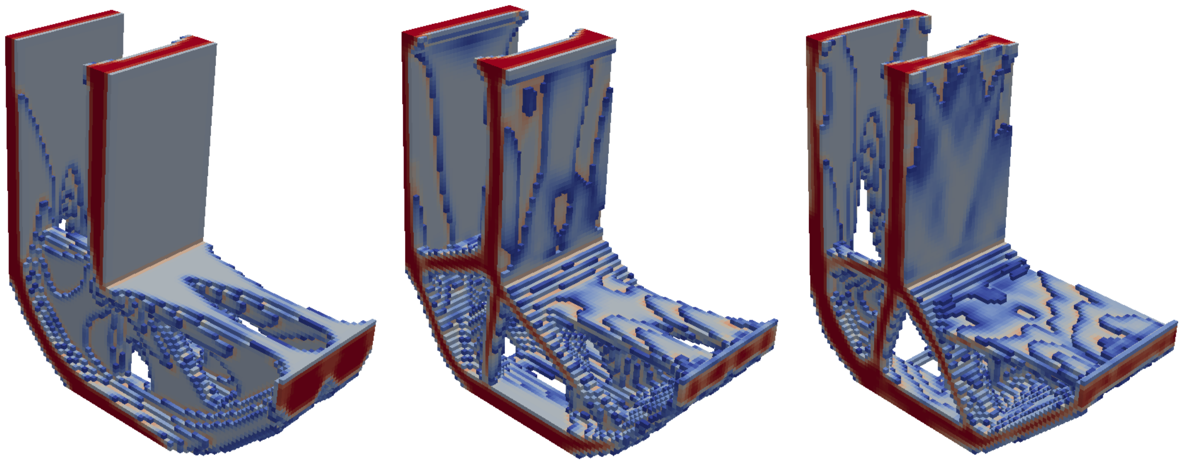

(a) Compliance minimization - Volume fraction

(b) Mass minimization - Von Mises

(c) Mass minimization - Fatigue (signed von Mises)

Figure 6.13: Density distribution illustrated for $\tilde{\rho}_e \geq 0.5$ - Isoview

Figure 6.12 and 6.13 which illustrate the physical density distribution of the three topology optimization formulations, facilitate comparison between the various formulations. Considering the minimum compliance problem 6.12a it can be seen the re-entrant corner still is present, since the stress concentration which arises does not effect the minimum compliance problem. Comparing that to the other two formulations which are based on stress constraints, the von mises yield constraint in figure 6.12b and a fatigue constraint based on the signed von Mises criterion in figure 6.12c. Here it can be seen that the geometry is curved in the vicinity of the re-entrant corner, in order to reduce the effect of the stress concentration.

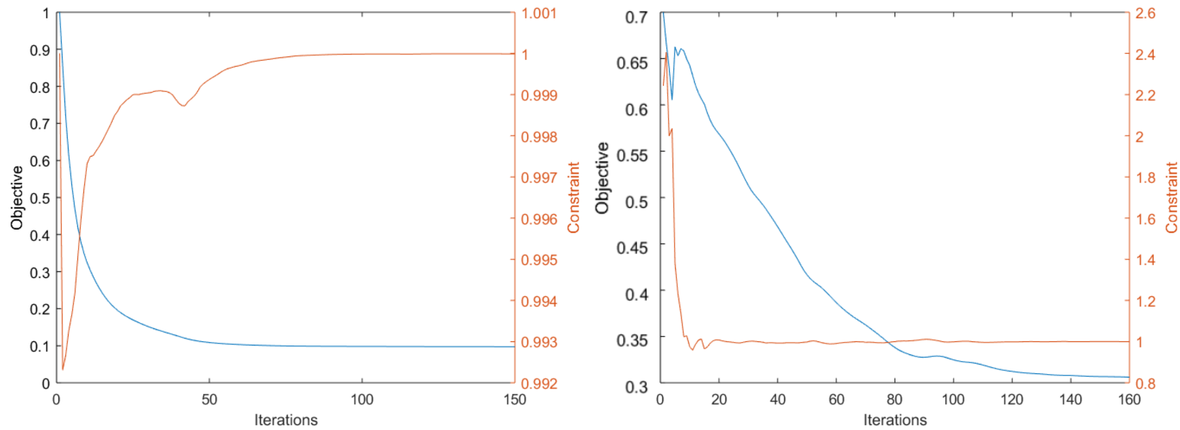

(a) Compliance minimization
- Volume constraint

(b) Mass minimization
- Von Mises constraint

Figure 6.14: Iteration History

Figure 6.14 illustrates the iteration history for the normalized minimum compliance problem, and for the mass minimization subjected to a yield constraint. From the iteration history it can be noted how quickly the optimizations problems converged, and how the iteration history is quite smooth for both formulations.

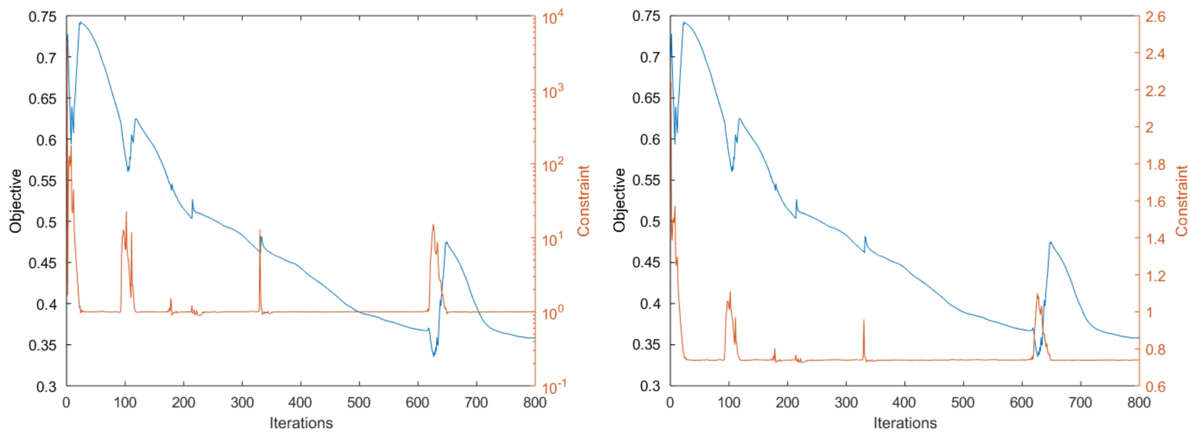

(a) Mass minimization
- Fatigue (signed von Mises) constraint

(b) Mass minimization
- Von Mises constraint

Figure 6.15: Iteration history for combined yield and fatigue constraints

This is evident when comparing to figure 6.15 which illustrates the iteration history of the mass minimization with combined fatigue and yield constraints. Here three distinct jumps occur during the optimization, illustrated by the sudden constraint violation. This optimization also required 800 iterations in order to converge, compared to 150 for the compliance problem and 160 for mass minimization with a yield constraint. This further highlights the non-linear nature of fatigue constraints.

Stress & Damage Distribution

Illustrating the stress and damage distribution for 3D examples is not as straight forward as for 2D, since the stress or damage is generally highest in the center of the structure, and then gradually decrease due to the filtering techniques applied. Here the stress and damage distribution are illustrated by thresholding the stress and damage value, such that only stress and damage above a certain value is shown. Here the stress and damage distribution of the combined fatigue and yield constraint problem as illustrated in figure 6.12c is considered, where only values above 0.7 times either μ or σ_{lim} for damage or von Mises stress, respectively, are shown.

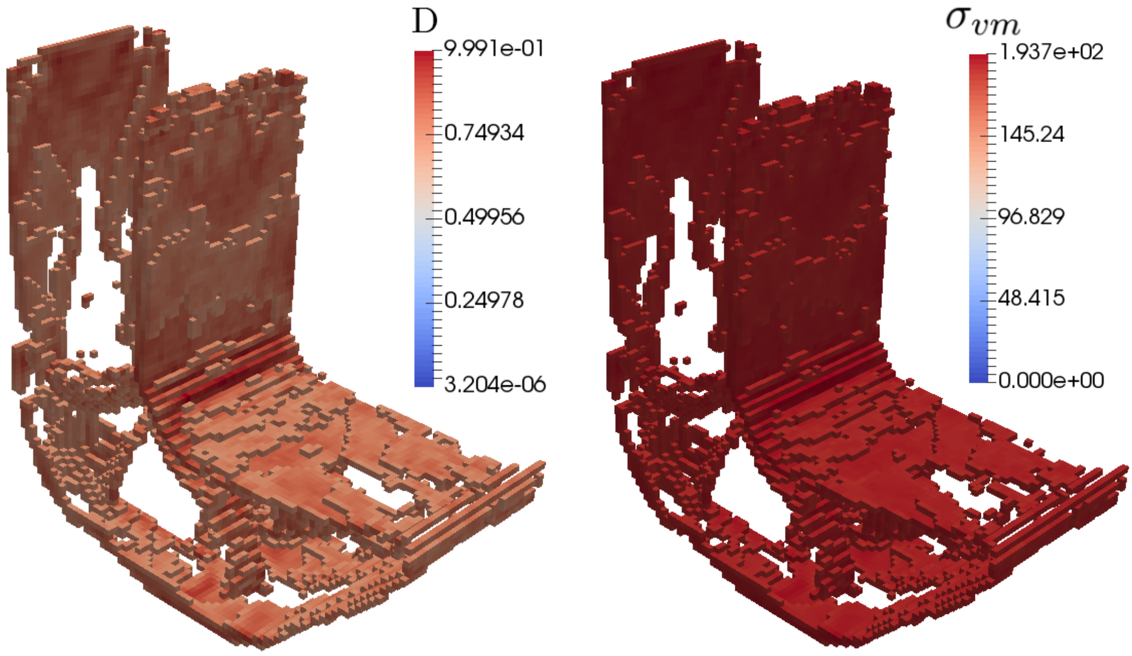

(a) Damage distribution $> 0.7\ \mu$ (b) Von Mises stress distribution $> 0.7\ \sigma_{lim}$

Figure 6.16: Damage and von Mises stress distribution

Considering the damage distribution illustrated in figure 6.16a it can be seen that there are many damage values above 0.7μ distributed over the structure. There is a concentration of higher damaged elements around the stress concentration, which occurs due to the re-entrant corner. The von Mises stresses in figure 6.16b are also distributed well over the structure.

Large Discretization

In industrial applications, a large discretization is often necessary in order to achieve sufficient representability. Furthermore, the large discretization allows for more detailed structures. The following example illustrates the use of the established formulations in large scale optimization considering a combined yield and fatigue constraint based on the signed von Mises. Here the L-beam is discretized using $n_e = 1048576$ 1mm elements and a filter radius of 4.8 element lengths. It is solved for $F_{ref} = 25000N$ for k = 1000 number of loads with r = -1, and the load history is scaled with $c_d = 5000$.

The following figure illustrates the L-beam in an isometric view, with only densities above 0.5 shown.

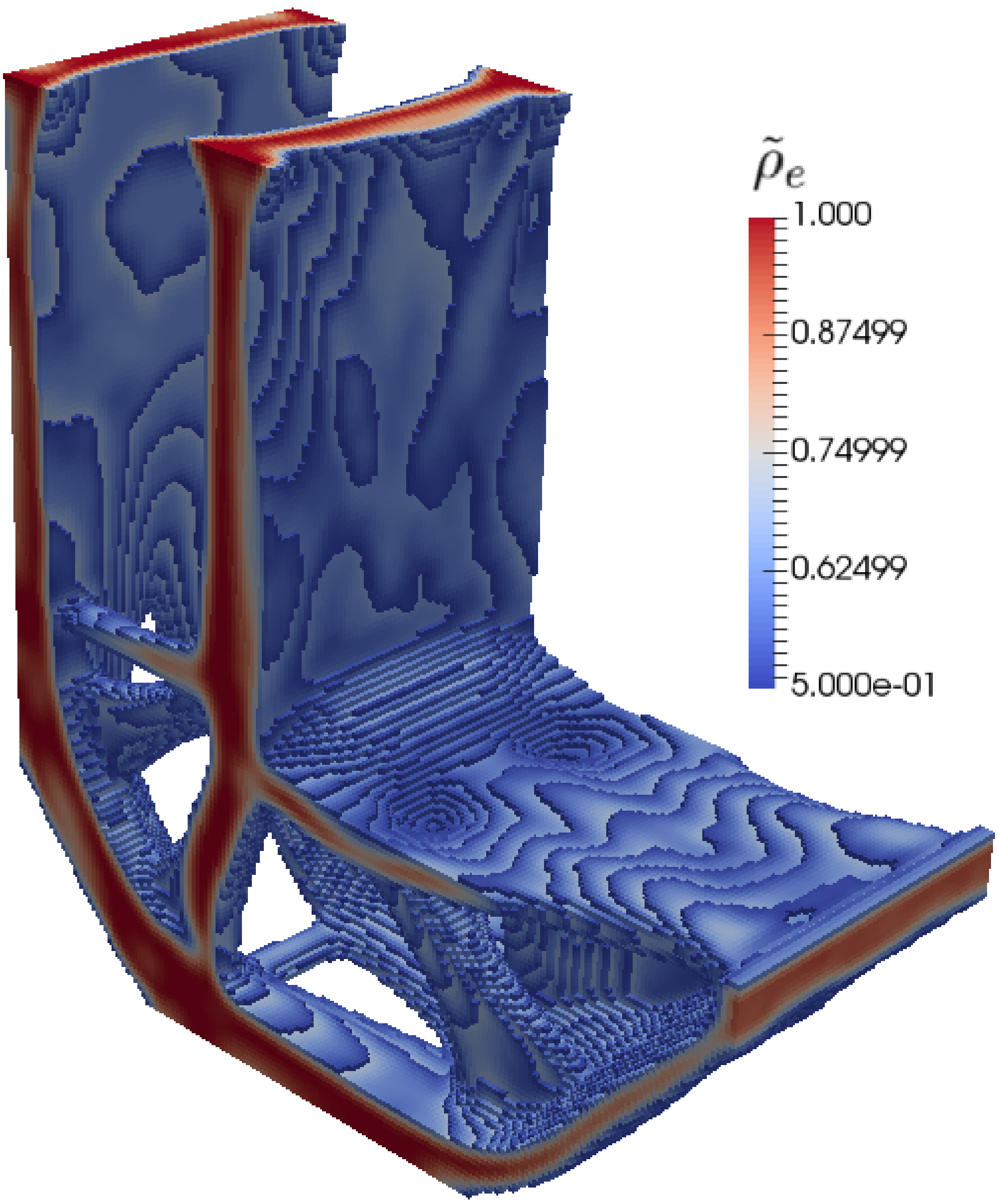

Figure 6.17: Isometric view L-beam

Considering figure 6.18 it can be seen that the optimized structure is relatively symmetrical. Figure 6.17 can be compared with the L-beam example in the previous section illustrated in figure 6.13c which was solved using 1/8 the amount of elements.

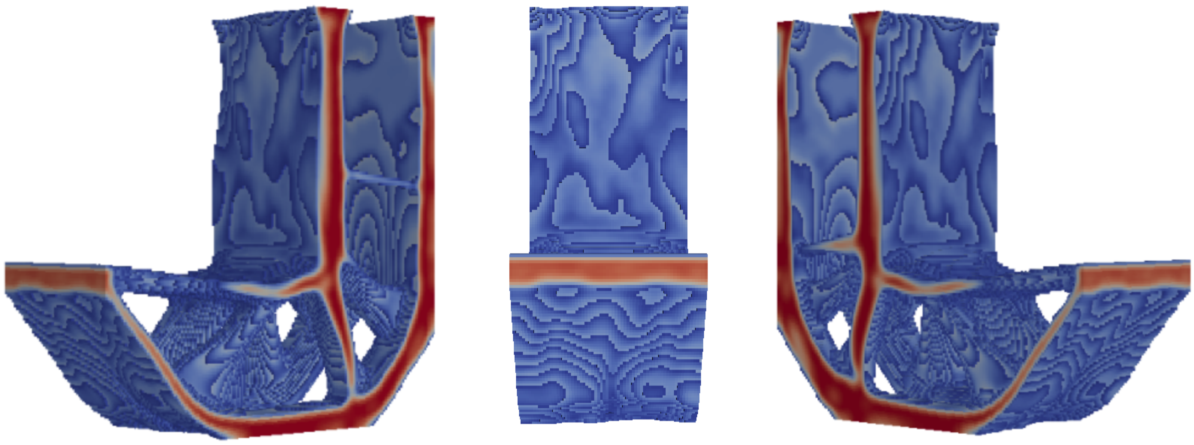

Figure 6.18: Side and front view

In figure 6.19 the iteration history for the large discretization is shown. It is quite similar to the iteration history for the previous example shown in figure 6.15, however, there are a few more jumps in the iteration history and larger constraint violations. This might be due to the finer discretization.

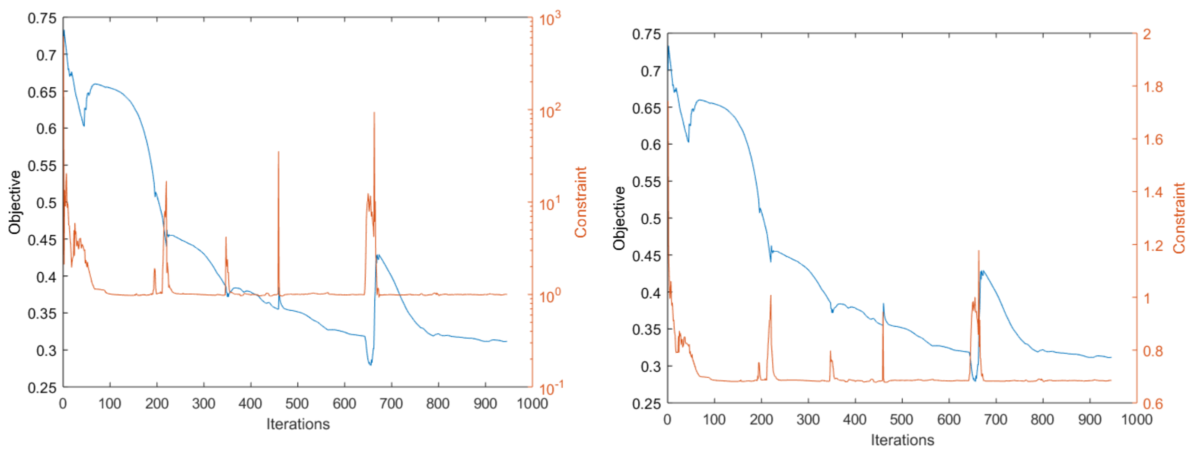

(a) Iteration history - Fatigue (signed von Mises) constraint

(b) Iteration history - Von Mises constraint

Figure 6.19: Iteration history for combined fatigue (signed von Mises) and von Mises constraint

6.5 Threshold Filtering

The following section examines the use of threshold filtering as outline in section 2.1.2, when considering mass minimization subjected to combined yield and fatigue constraints based on Sines criterion. The transition zone from solid to void which inevitably arises from using the linear decaying density filter, is generally undesirable since intermediate density values have no physical meaning. This motivates the use of a projection filter, which creates more solid/void structures, in order to minimize post optimization processing. However, using the threshold filter introduces a large non-linearity into an already very non-linear optimization problem. The threshold filter will here be illustrated on a cantilever beam illustrated in figure 6.2b. This benchmark example was chosen, since it is generally easier to solve due to the fact that it does not contain any re-entrant corners. Therefore, the non-linearity of the threshold filter can be illustrated more clearly. Here the threshold value $\eta = 0.5$ is chosen, since an η value at either extreme of 0 and 1 is more unstable, and based on experience $\eta = 0.5$ is the most stable.

As mentioned previously here the cantilever beam example is used. It is subjected to a reference force of $F_{ref} = 25000N$, with a load ratio of $r = -1$ for k = 1000 and the load history is scaled with $c_d = 5000$. The domain is discretized using $n_e = 524288$ 1mm elements, and a filter radius of 3.2 element lengths. Furthermore, tighter move limits of 0.5 is set.

When presenting topology optimization results in 3D, usually only values density values above 0.5 are shown (Aage et al., 2015; Jeong et al., 2013). The following picture illustrates the optimized structure for densities above 0.1, 0.5 and 0.9.

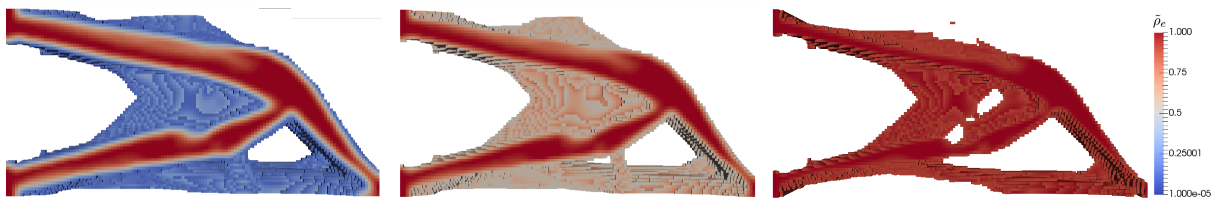

Figure 6.20: Densities above 0.1, 0.5 and 0.9 with the density filter - Side view

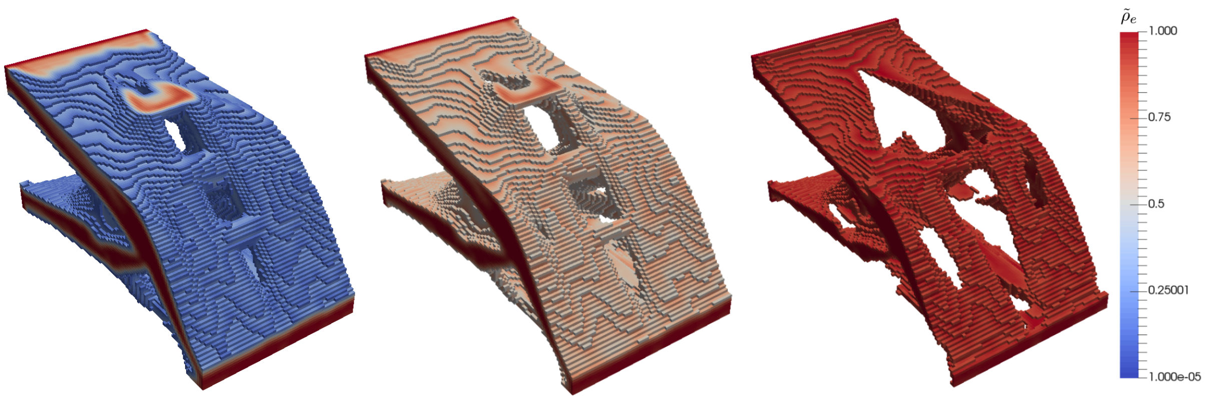

Figure 6.21: Densities above 0.1, 0.5 and 0.9 with the density filter - Iso view

In figures 6.20 and 6.21 the transition zone between solid (red color) and void (blue color) is visible as different density values are shown. Considering the iteration history in figure 6.22 it can be seen that the convergence is relatively stable, with only minor constraint violations during the optimization.

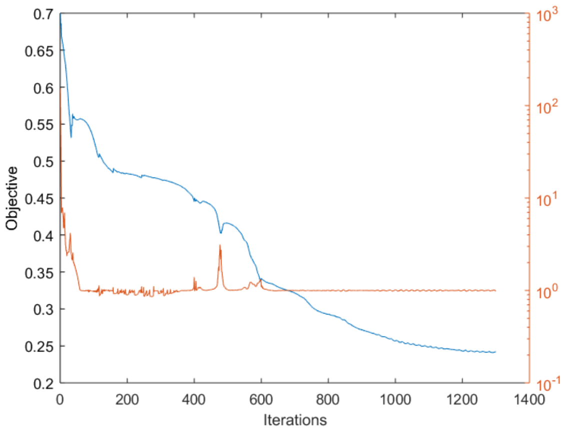

(a) Iteration history - Fatigue (Sines) constraint

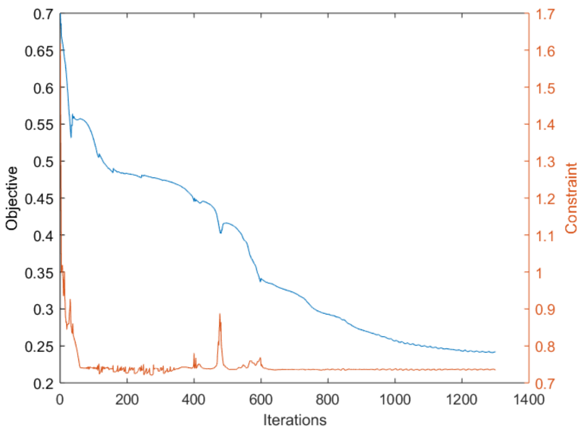

(b) Iteration history - Von Mises constraint

Figure 6.22: Iteration history for combined fatigue (Sines) and von Mises constraint with the density filter

In the following example the threshold filter is applied. The same problem is solved for the same settings, as outlined previously. However, here the β value used in (2.10) is set to a very small value for the initial iterations. Then after the optimization has converged, is the β value updated. The β value is initially updated to 0.5, and then subsequently updated every 30^{th} iteration if the constraints are not violated, by first updating β to 1 and then by adding 1 to the current β value. The following figures 6.23 and 6.24 likewise illustrates the optimized structure for densities above 0.1, 0.5 and 0.9, after using the threshold filter. Comparing these figures to figure 6.20 and 6.21 it can be seen that it has the same topological structure and there is far more high value densities nearer the surface of the structure, due to the projection filter.

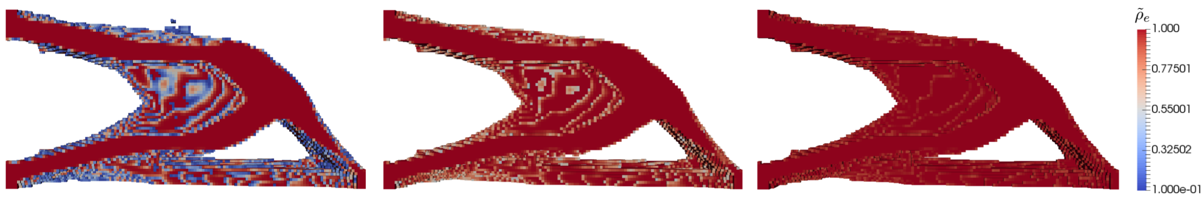

Figure 6.23: Densities above 0.1, 0.5 and 0.9 with the threshold filter - Side view

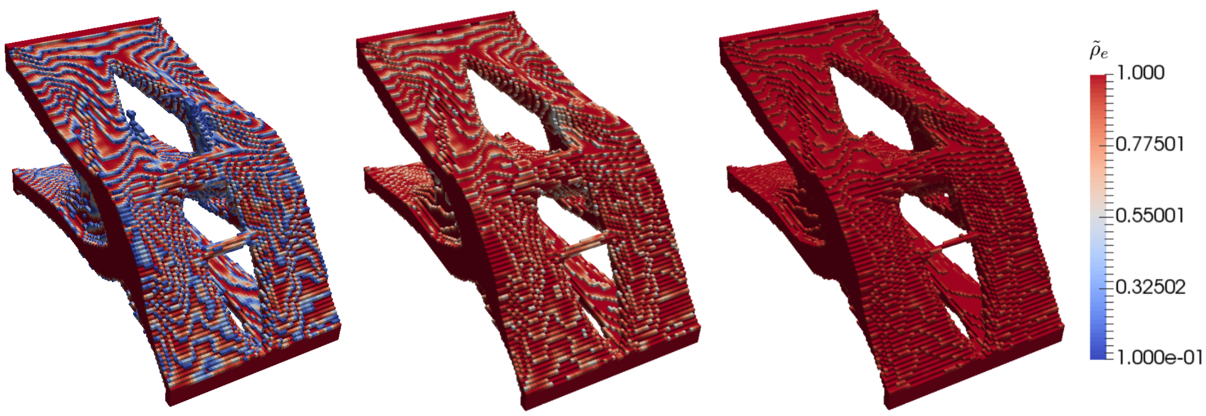

Figure 6.24: Densities above 0.1, 0.5 and 0.9 with the threshold filter - Iso view

Referring to the iteration history in figure 6.30, the effect of the threshold filter is clearly visible. Here it can be seen that updating the β value starts at approximately iteration 1250, and each time β is increased a constraint violation occurs followed by an increase in the objective function in order to reduce the constraint violation.

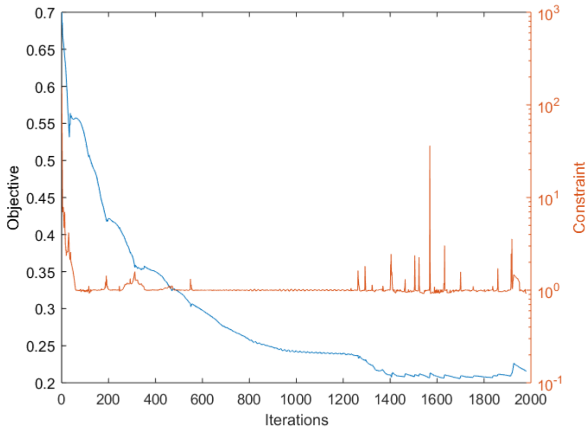

(a) Iteration history - Fatigue (Sines) constraint

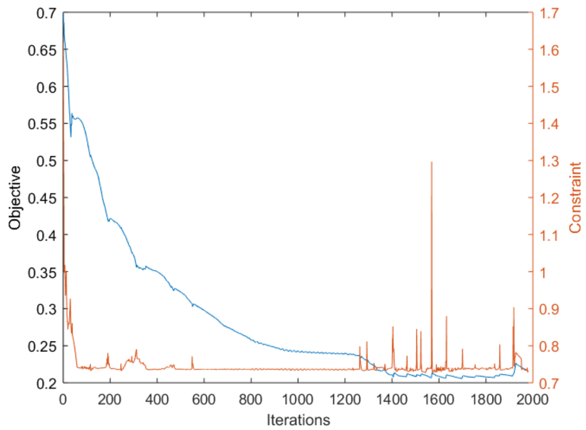

(b) Iteration history - Von Mises constraint

Figure 6.25: Iteration history for combined fatigue (Sines) and von Mises constraint with the threshold filter filter

Figure 6.26 show the damage distribution for the two examples, where the left figure is with the density filter and the right figure with the threshold filter. Here it can be seen that there are more high damage elements in figure 6.26a compared with 6.26b. This might be due to the higher element density when using the threshold filter, which reduces the damage in an element as compared with low density elements.

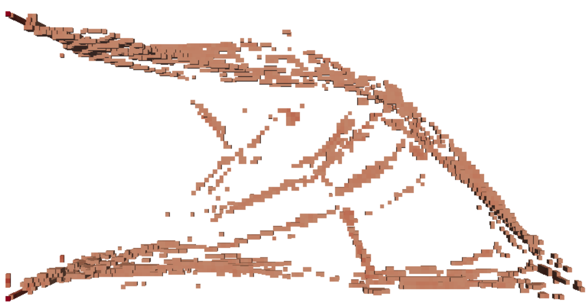

(a) Damage > 0.7 μ with density filter

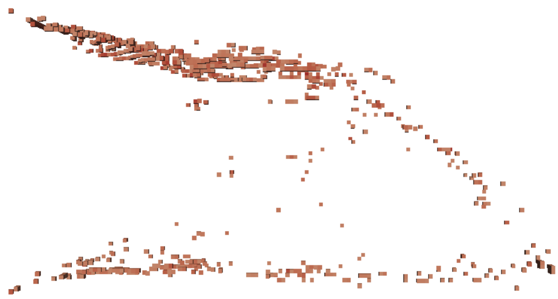

(b) Damage > 0.7 μ with threshold filter

Figure 6.26: Damage distribution

The optimization was stopped at iteration 1980 since a sufficiently low discreteness level was reached. The presented example is solved under the best conditions. It is solved for an easy benchmark example, with combined fatigue and yield constraints, which have a positive effect on convergence, the η value is set in the middle of either extreme, β is updated very late in the optimization and in very small steps and with tighter move limits. Through numerical experiments with applying the threshold filter, it has been found to greatly increase the difficulty of solving the optimization problems, due to large instabilities. This instability might be due to the fact that as β increase, the derivative of the threshold filter (5.4) approaches the Dirac delta function and creates very large gradients. There are methods which might minimize the non-linear effects of the threshold filter. The β value might be updated in smaller steps with larger intervals, or the aggregation parameter P might be lowered, reducing the overall non-linearity of the optimization problem as proposed in Oest and Lund (2017a).

The benefit of more solid/void structures which the threshold filter provides, comes with a price of a more difficult problem to solve, and as evident when comparing the iteration histories, requires many more iterations in order to convergence, and thus increased solution time. There are many parameters which are relevant when solving topology optimization with threshold filtering, all of which can have a great influence in the final result, especially when considering fatigue constraints which are already characterized by highly non-linear behaviour.

6.6 Curved Beam

A reason for the computational efficiency of the topology optimization formulated in the PETSc framework, is that it utilizes structured grids. Structured grids are characterized by regular connectivity of the elements, and a domain defined on Cartesian axis. As mentioned previously this domain can be modified while still maintaining the connectivity. This example is of a curved beam where a cantilever beam defined on Cartesian axis is curved. This distorts the elements and therefore requires the use of isoparametric elements, furthermore due to the distortion the element stiffness matrix and the strain-displacement matrix has to established for each element.

The curved beam is solved for a combined fatigue and yield constraint, where the fatigue constraint is based on signed von Mises. The domain is discretized using n_e = 131072 1mm elements with a filter radius of 2.4 element lengths. The curved beam is subjected to a force of $F_{ref} = 5000N$ with fully reversed loading, k =1000 and the load history is scaled by $c_d = 1000$.

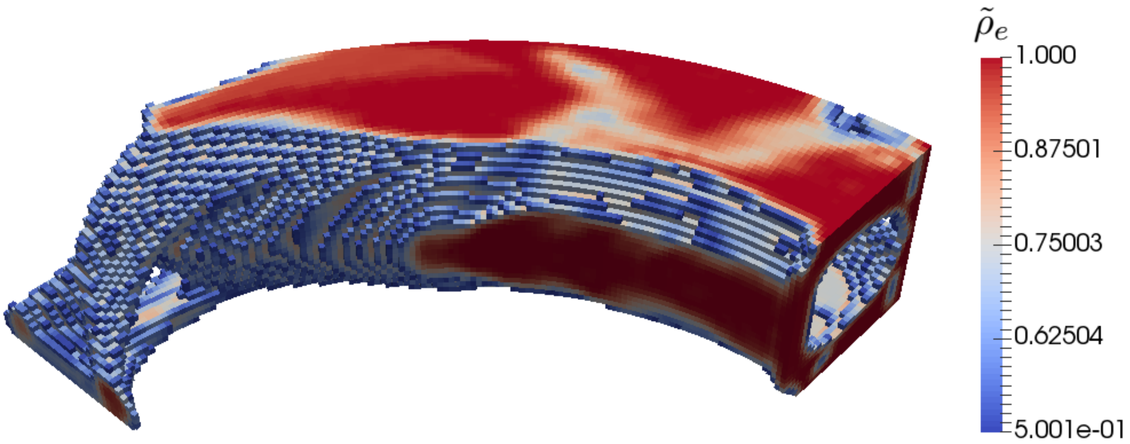

Figure 6.27: Density distribution illustrated for $\tilde{\rho}_e \geq 0.5$ for the curved beam - Isoview

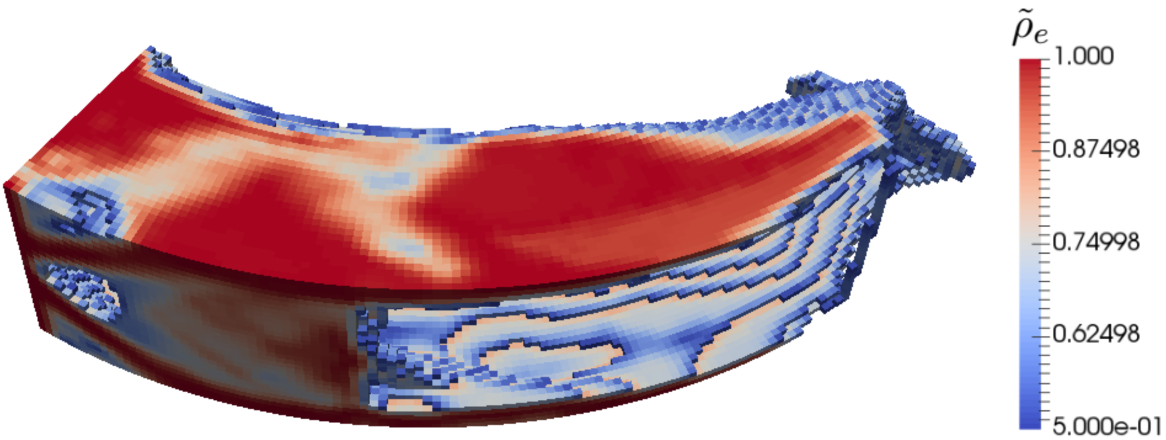

Figure 6.28: Density distribution illustrated for $\tilde{\rho}_e \geq 0.5$ for the curved beam - Isoview

Figure 6.27 illustrates the optimized result. As can be seen at the loaded end of the curved beam, the optimized result resembles a cantilever beam, while at the support a hollow tube, this is further illustrated in figure 6.29.

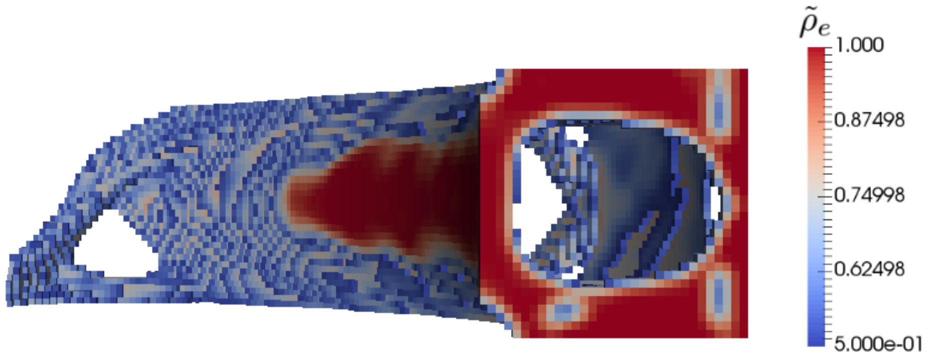

Figure 6.29: Density distribution illustrated for $\tilde{\rho}_e \geq 0.5$ for the curved beam - Backview

The curved beam was comparatively hard to solve, and required a lower P value of 10, as well as tighter move limits of 0.025. Due to time restrictions, the filtering of the curved beam was calculated based on the undeformed geometry, and thus not completely accurate. This might account for the issues of convergence as illustrated in the following iteration history.

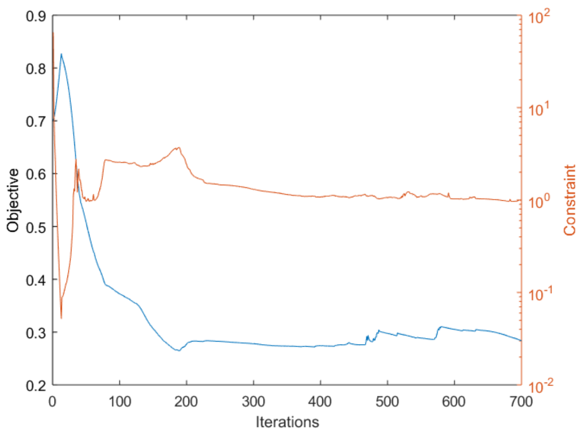

(a) Iteration history - Fatigue (signed von Mises) constraint

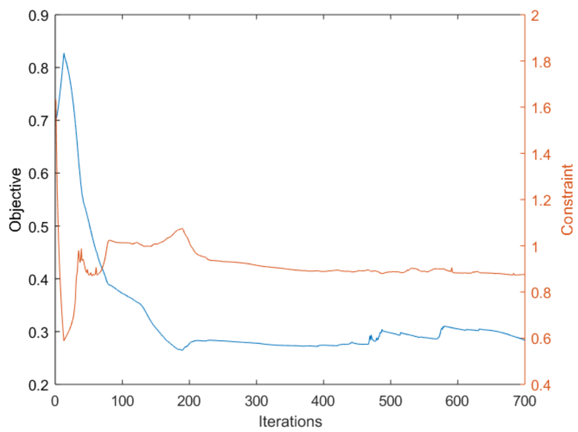

(b) Iteration history - Von Mises constraint

Figure 6.30: Iteration history for combined Sines and von Mises constraint

As can be seen in figure 6.30a the fatigue constraint is violated during most of the optimization procedure, as compared with the previously presented iteration histories, where the constraint is generally satisfied. The optimization procedure was here stopped when the constraints were not violated. The damage and von Mises stress distribution are shown in figure 6.31.

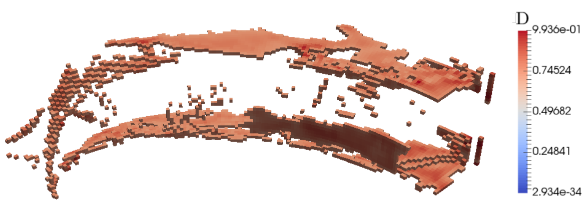

(a) Damage distribution > 0.7 μ

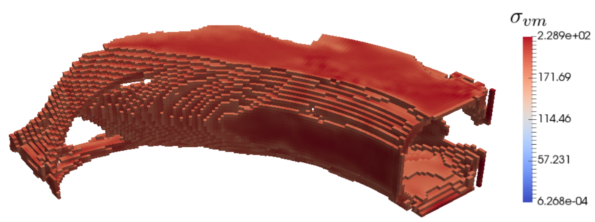

(b) Von Mises stress distribution > 0.7 σ_{lim}

Figure 6.31: Damage and von Mises stress distribution for curved beam

7 Conclusion & Summary

As stated in the introduction, the objective of this thesis was to solve large-scale topology optimization with a minimum mass objective and subjected to fatigue and yield constraints. This goal was set in order to increase the applicability of topology optimization in an industrial setting, as mass minimization is a general aim across numerous industries for various reasons. Many structures are subjected to variable loading, and as a result may fail due to fatigue. A yield constraint is a general requirement for most structures, and within the context of high cycle fatigue, a necessity not to violate some basic assumption within the fatigue analysis.

Both the desired constraints are established based on the stresses which occurs in the structure during loading. Constraints based on stresses creates well known issues within topology optimization, due to the local quantity of a stress state and the singular optima that arises. The problem of the singular optima can be solved using various methods, the method utilized here is the qp-method.

The locality of stress constraints is especially relevant when conducting large-scale optimization, which for the examples presented in this thesis would result in more than a million constraints. The computational resources necessary to solve such a problem would be immense. In order to solve a problem of sufficient size in a reasonable amount of time, the P-norm aggregate function was implemented. The aggregate function, in this implementation, converts all the local constraints into a single representative constraint, such that only one constraint has to be satisfied. This greatly reduces the computational time and allows for the solution of large scale problems.

The fatigue constraints are formulated directly in the topology optimization. The constraints are formulated based on assumptions of proportional loading with a variable amplitude in the high cycle domain. The multiaxial stress state which occurs are converted to an equivalent uniaxial amplitude stress by employing either the Sines method or signed von Mises with the mean stress effects accounted for by using the modified Goodman equation. From this equivalent uniaxial amplitude stress the number of cycles to failure can be estimated by employing the Basquin curve, and from there the fatigue constraint can be formulated by introducing the notion of element wise damage through the Palmgren-Miners linear damage hypothesis. Like the yield constraint, the damage constraint is a local quantity, such that the aggregate function is likewise utilized.

In order to solve the topology optimization in an efficient manner gradient based optimization methods are utilized. Here, the first order version of the MMA optimizer is used, where the gradients are analytically determined using the adjoint formulation.

These topology optimization formulations were illustrated in a number of examples, some to illustrate the complications associated with including fatigue constraints, such as the added non-linearity and the possible violation of linear elastic behaviour if not combined with a yield constraint. Other examples were included to highlight the applicability of the formulations in a more realistic setting, which requires a large number of elements in order to have sufficient representability. Here the examples included discretizations of up to one million elements. Furthermore, the application of the threshold filter was illustrated for the cantilever beam benchmark example, and the difficulty that it procedures was highlighted.

The specific topology optimization formulation used, is based on a number of assumptions, which if violated result in unsuitable solutions. The fatigue constraints are formulated assuming quasi-static loading, such that the inertial effects can be neglected, proportional loading is assumed and the structure is considered to be linear elastic.

Topology optimization with fatigue constraints is characterized by high non-linearity which results in problems that can be difficult to solve, and as stated in the introduction, topology optimization is no silver bullet for the problems of structural design. There are many nuances to take into account, and many user specified parameters which can have a great influence on the final solution. The goal of this thesis was to perform large-scale topology optimization in 3D with industrially relevant constraints, in order to move the field of topology optimization closer to industrial applicability.

Future work within this area could entail further study into the use of projection filters. The benefit of obtaining solid/void structures during the optimization, such that the post optimization processing is minimized is desirable, however the added difficulty of obtaining a solution requires longer solution times and careful parameter setting. Using the fixed mesh with rectangular and brick elements produces jagged edges on the structure. This jagged surface, as noted in Svärd (2015b), causes non-physical stress concentrations at the surface. He proposed using an interior value extrapolation, which resulted in a more stable and accurate stress measure. Due to the sensitivity of fatigue constraints, this might reduce some of the unstable behaviour. Lastly, the structures generated here have, as previously mentioned, jagged edges which should be smoothed as part of post optimization processing. An automated way of performing this smoothing which also can parametrize the topology optimized structure, such that shape optimization can be performed afterwards, could further reduce the need for human post optimization processing.

References

Aage, N., E. Andreassen, and B. S. Lazarov (2015). Topology optimization using PETSc: An easy-to-use, fully parallel, open source topology optimization framework. *Structural and Multidisciplinary Optimization 51*(3), 565–572.

Aage, N., E. Andreassen, B. S. Lazarov, and O. Sigmund (2017). Giga-voxel computational morphogenesis for structural design. *Nature 550*(7674), 84–86.

Aage, N. and B. S. Lazarov (2013). Parallel framework for topology optimization using the method of moving asymptotes. *Structural and Multidisciplinary Optimization 47*(4), 493–505.

Andreassen, E., A. Clausen, M. Schevenels, B. S. Lazarov, and O. Sigmund (2011). Efficient topology optimization in MATLAB using 88 lines of code. *Structural and Multidisciplinary Optimization 43*(1), 1–16.

Bendsøe, M. and O. Sigmund (2003). *Topology Optimization: Theory, Methods, and Applications*. Springer-Verlag Berlin Heidelberg Gmb.

Bendsøe, M. P. (1989). Optimal shape design as a material distribution problem. *Structural Optimization 1*(4), 193–202.

Bendsøe, M. P. and N. Kikuchi (1988). Generating optimal topologies in structural design using a homogenisation method. *Computer Methods in Applied Mechanics and Engineering 71*(2), 197–224.

Bendsøe, M. P. and O. Sigmund (1999). Material interpolation schemes in topology optimization. *Archive of Applied Mechanics (Ingenieur Archiv) 69*(9-10), 635–654.

Blackwell, E., T. Gambell, V. Marya, C. Schmitz, C. Melrose, and J. Tilley (2017). The great re-make : Manufacturing for modern times. Technical Report June.

Bourdin, B. (2001). Filters in topology optimization. *International Journal for Numerical Methods in Engineering 50*(9), 2143–2158.

Bruggi, M. (2008). On an alternative approach to stress constraints relaxation in topology optimization. *Structural and Multidisciplinary Optimization 36*(2), 125–141.

Bruns, T. E. and D. A. Tortorelli (2001). Topology optimization of non-linear elastic structures and compliant mechanisms. *Computer Methods in Applied Mechanics and Engineering 190*(26-27), 3443–3459.

Cheng, G. and G. Xu (1997). epsilon-relaxed approach in structural topology optimization. *Structural Optimization 13*(1972), 258–266.

Chin, T. W. and G. J. Kennedy (2016). Large-Scale Compliance-Minimization and Buckling Topology Optimization of the Undeformed Common Research Model Wing. *57th AIAA/ASCE/AHS/ASC Structures, Structural Dynamics, and Material Conference* (January), 1–18.

Christensen, P. W. and A. Klabring (2009). *An introduction to structural optimization.* Springer Netherlands.

Clausen, A. and E. Andreassen (2017). On filter boundary conditions in topology optimization. *Structural and Multidisciplinary Optimization 56*(5), 1147–1155.

Collet, M., M. Bruggi, and P. Duysinx (2017). Topology optimization for minimum weight with compliance and simplified nominal stress constraints for fatigue resistance. *Structural and Multidisciplinary Optimization 55*(3), 839–855.

Cook, R. D., D. S. Malkus, M. E. Plesha, and R. J. Witt (2001). *Finite Element Analysis.* John Wiley & Sons.

Díaz, A. and O. Sigmund (1995). Checkerboard patterns in layout optimization. *Structural Optimization 10*(1), 40–45.

Duysinx, P. and M. P. Bendsøe (1998). Topology optimization of continuum structures with local stress constraints.

Dym, C. and I. Shames (2013). Solid Mechanics - A variational Approach.

Guest, J. K., J. H. Prévost, and T. Belytschko (2004). Achieving minimum length scale in topology optimization using nodal design variables and projection functions. *International Journal for Numerical Methods in Engineering 61*(2), 238–254.

Holmberg, E. (2016). *Topology optimization considering stress, fatigue and load uncertainties.* Ph. D. thesis, Linkoping University.

Holmberg, E., B. Torstenfelt, and A. Klarbring (2013). Stress constrained topology optimization. *Structural and Multidisciplinary Optimization 48*(1), 33–47.

Holmberg, E., B. Torstenfelt, and A. Klarbring (2014). Fatigue constrained topology optimization. *Structural and Multidisciplinary Optimization 50*(2), 207–219.

Jeong, S. H., D. H. Choi, and G. H. Yoon (2015). Fatigue and static failure considerations using a topology optimization method. *Applied Mathematical Modelling 39*(3-4), 1137–1162.

Jeong, S. H., S. H. Park, D. H. Choi, and G. H. Yoon (2013). Toward a stress-based topology optimization procedure with indirect calculation of internal finite element information. *Computers and Mathematics with Applications 66*(6), 1065–1081.

Krog, L., A. Tucker, and G. Rollema (2002). Application of topology, sizing and shape optimization methods to optimal design of aircraft components. *3rd Altair UK HyperWorks Users Conference*, 1–12.

Le, C., J. Norato, T. Bruns, C. Ha, and D. Tortorelli (2010). Stress-based topology optimization for continua. *Structural and Multidisciplinary Optimization 41*(4), 605–620.

Lee, J. W., G. H. Yoon, and S. H. Jeong (2015). Topology optimization considering fatigue life in the frequency domain. *Computers and Mathematics with Applications 70*(8), 1852–1877.

Matthias Penzel (2015). Porsche Engineering Magazine. (1), 7–8.

Norton, R. L. (2011). *Machine Design. An Integrated Approach.* Prentice Hall.

Oest, J. (2017). *Structural Optimization with Fatigue Constraints*. Ph. D. thesis, Aalborg Universitet.

Oest, J. and E. Lund (2017a). Finite-life fatigue constraints in 2D topology optimization of continua. In *30th Nordic Seminar on Computational Mechanics (NSCM-30)*, pp. 25–27.

Oest, J. and E. Lund (2017b). Topology optimization with finite-life fatigue constraints. *Structural and Multidisciplinary Optimization 56*(5), 1045–1059.

Sigmund, O. (1997). On the design of compliant mechanisms using topology optimization. *Mechanics of Structures and Machines 25*(4), 493–524.

Sigmund, O. (2007). Morphology-based black and white filters for topology optimization. *Structural and Multidisciplinary Optimization 33*(4-5), 401–424.

Sigmund, O. (2011). On the usefulness of non-gradient approaches in topology optimization. *Structural and Multidisciplinary Optimization 43*(5), 589–596.

Sigmund, O., N. Aage, and E. Andreassen (2016). On the (non-)optimality of Michell structures. *Structural and Multidisciplinary Optimization 54*(2), 361–373.

Sigmund, O. and K. Maute (2013). Topology optimization approaches: A comparative review. *Structural and Multidisciplinary Optimization 48*(6), 1031–1055.

Sigmund, O. and J. Petersson (1998). Numerical instabilities in topology optimization: A survey on procedures dealing with checkerboards, mesh-dependencies and local minima. *Structural Optimization 16*(1), 68–75.

Stephens, R. I., A. Fatemi, R. R. Stephens, and H. O. Fuchs (2001). *Metal Fatigue in Engineering* (Second ed.). John Wiley & Sons.

Stolpe, M. (2003). *On Models and Methods for Global Optimization of Structural Topology*. Ph. D. thesis, Royal Institute of Technology.

Svanberg, K. (1987). The method of moving asymptotes a new method for structural optimization. *International Journal for Numerical Methods in Engineering 24*(2), 359–373.

Svanberg, K. (2007). MMA and GCMMA – two methods for nonlinear optimization. Technical report, KTH, Stockholm.

Svärd, H. (2015a). A branch and bound algorithm for evaluation of the Findley fatigue criterion. *International Journal of Fatigue 73*, 27–38.

Svärd, H. (2015b). Interior value extrapolation: a new method for stress evaluation during topology optimization. *Structural and Multidisciplinary Optimization 51*(3), 613–629.

Sved, G. and Z. Ginos (1968). Structural optimization under multiple loading. *International Journal of Mechanical Sciences 10*(10), 803–805.

Verbart, A. (2015). *Topology Optimization With Stress Constraints*. Ph. D. thesis, TU Delft.

Wang, F., B. S. Lazarov, and O. Sigmund (2011). On projection methods, convergence and robust formulations in topology optimization. *Structural and Multidisciplinary Optimization 43*(6), 767–784.

Xu, S., Y. Cai, and G. Cheng (2010). Volume preserving nonlinear density filter based on heaviside functions. *Structural and Multidisciplinary Optimization 41* (4), 495–505.